Computers and Geotechnics 203 (2027) 108762

Contents lists available at ScienceDirect

Computers and Geotechnics

journal homepage: www.elsevier.com/locate/compgeo

Research Paper

Incremental homogenisation of anisotropic porous media with evolving solid contact using a finite-element-based linear complementarity framework

L. Zhang [a,b], N.A. Collins-Craft [a,c], P. Braun [a,*]

[a] Laboratoire Navier, Ecole Nationale des Ponts et Chaussees, Institut Polytechnique de Paris, Universite Gustave Eiffel, CNRS, 6–8 Avenue Blaise Pascal, Champs-sur-Marne, 77455, France
[b] GEOMAR Helmholtz Centre for Ocean Research, Wischhofstraße 1-3, Kiel, 24148, Germany
[c] School of Mathematics, Statistics, Chemistry and Physics, Murdoch University, 90 South Street, Murdoch, 6150, Western Australia, Australia

ARTICLE INFO

Keywords:
Anisotropic porous structure
Incremental homogenisation
Solid contact
Finite element method
Perturbation-based stiffness updating

ABSTRACT

The mechanical response of porous materials undergoing pore closure is strongly influenced by the progressive activation of solid–solid contact, which produces anisotropic and path-dependent effective properties that are difficult to capture using classical homogenisation approaches. This work presents a finite-element-based incremental framework for computing the evolving tangent effective response of two-dimensional porous media under plane-strain conditions, explicitly accounting for frictionless contact between pore boundaries. The framework combines segment-to-segment contact, periodic boundary conditions, updated geometrical configurations, and a perturbation procedure for evaluating tangent stiffness along the deformation path. After finite element discretisation, the unilateral contact conditions lead to linear complementarity problems that must be solved repeatedly as the contact topology evolves, making conventional LCP solvers a potential computational bottleneck. Its primary methodological contribution is a fast approximation method for these linear complementarity problems, denoted FA-LCP. In the benchmark cases considered, FA-LCP reduces the contact-solution time by one to two orders of magnitude relative to the Lemke and projected Gauss–Seidel algorithms, while reproducing their global contact forces and homogenised stiffnesses within the reported numerical tolerances and requiring comparable memory.

Applications to single-pore and multi-pore geometries demonstrate how contact onset, progressive pore closure, and contact-network development modify directional stiffness and inferred Biot coefficients. The results reveal a transition from skeleton-controlled deformation to contact-network-dominated behaviour, showing that the evolution of directional tangent properties is governed by contact-network development rather than by changes in porosity alone. The proposed method provides an efficient tool for evaluating contact-driven changes in the homogenised tangent properties of porous solids and offers a basis for future multiscale finite element applications.

1. Introduction

The mechanical behaviour of anisotropic porous materials plays an important role for the safe and efficient design of subsurface engineering applications, such as geological CO_2 sequestration, hydrogen storage, geohazard mitigation, and unconventional hydrocarbon extraction. To model and predict hydromechanical behaviour of rocks in the poroelasticity framework, macroscopic properties such as Young's modulus, shear modulus, and Biot coefficients are required. Microstructural evolution of porosity, solid–solid contact interactions, and structural anisotropy of the material collectively govern these macroscopic hydromechanical characteristics (Biot, 1973; Sahimi, 1993). Such evolution encompasses pore partitioning and fracture initiation (Lee et al., 2019), fracture closure and opening dynamics (Batzle et al., 1980) and pore clogging with resultant permeability alterations (Tang et al., 2020). Accurate prediction of how pore geometry and pore-wall contact evolve under deformation is therefore essential for estimating the tangent elastic and poromechanical properties used in multiscale modelling of porous media.

The deformation of porous microstructures has long been studied within poroelasticity and homogenisation frameworks (Biot, 1941; Coussy, 2004). Changes in pore shape, pore closure and pore-wall interaction can substantially modify the effective response of the porous skeleton (Ponte Castañeda and Zaidman, 1994). When opposing pore surfaces come into contact, the relevant mechanical problem is unilateral frictionless solid–solid contact at the microscale. Such contact is naturally expressed through non-penetration and complementarity

* Corresponding author.
E-mail address: philipp.braun@enpc.fr (P. Braun).

https://doi.org/10.1016/j.compgeo.2026.108762
Received 10 July 2026; Received in revised form 24 September 2026; Accepted 15 October 2026
0266-352X/© 2026 Published by Elsevier Ltd.

conditions, and can be treated by variational inequalities, semi-smooth Newton formulations, or finite-dimensional complementarity problems after FE discretisation.

Among numerical approaches, FEM is well suited for the present objective because it can represent continuous deformation of complex pore geometries while providing a direct route to homogenised stiffness evaluation. In the FEM setting, unilateral contact can be enforced by penalty, Lagrange multiplier, augmented Lagrangian or nonsmooth complementarity-based formulations (Wriggers, 1995; Perić and Owen, 1992; Papadopoulos and Solberg, 1998; Yastrebov, 2013).

The present work adopts a nonsmooth complementarity viewpoint because it avoids artificial penalty stiffnesses and provides direct access to contact forces with high precision and numerical stability by rigorously enforcing the non-penetration constraint through set-valued functions (Yastrebov, 2013). This method is apt to be formulated in variational frameworks that demonstrate excellent energy-preservation properties (Capobianco and Eugster, 2016; Capobianco et al., 2017; Capobianco and Eugster, 2018; Acary et al., 2023). Further, nonsmooth mechanics formulations can often be transformed to favourable problem formulations arising from the optimisation community, of which the most favourable (and most frequent, as it arises in cases of contact between linear elastic bodies in geometrically linear frameworks) is the linear complementarity problem (LCP). However, while rigorous algorithms to obtain solutions of the LCP exist (such as Lemke's algorithm (Lemke and Howson, 1964; Lemke, 1965)), their computational complexity as the problem size increases can lead to high computational costs. Consequently, for multiscale simulations, an efficient solution strategy that maintains sufficient accuracy while avoiding excessive computational expense is highly desirable.

Homogenisation provides a way to derive effective material properties from microscale models while reducing the need for empirical calibration. Analytical approaches are available for idealised inclusion or pore geometries (Eshelby, 1957; Hill, 1965; Mori and Tanaka, 1973; Hashin, 1985), whereas numerical homogenisation is required for complex microstructures and evolving geometries (Kouznetsova et al., 2001; Geers et al., 2010; Kanouté et al., 2009). At the microscale, poroelastic coefficients depend on pore architecture, porosity and the properties of the solid phase (Lydzba and Shao, 2000; Tan and Koniet-zky, 2014; Ahmed et al., 2019; Dehghani and Zilian, 2020). However, when pore closure creates new solid–solid contacts, the homogenised response becomes path-dependent and must be updated as the contact topology evolves.

In multiscale FEM and RVE-based homogenisation, tangent effective properties must be evaluated repeatedly as the microstructure evolves (Miehe and Koch, 2002; Miehe, 2003; Kouznetsova et al., 2001; Temizer and Wriggers, 2008). Perturbation-based procedures provide a practical way to compute incremental stiffness coefficients directly from microscale simulations, but they are rarely combined with explicit updates of pore-wall contact topology. This limitation becomes important when pore closure or reopening changes the load-transfer paths within the skeleton.

Closely related work has been developed by Rohan and Heczko for homogenisation-based modelling of porous media with pore-scale unilateral self-contact (Rohan and Heczko, 2020, 2023, 2026). Their 2020 work addressed dry porous elastic microstructures and derived a two-scale model with a consistent effective tangent (Rohan and Heczko, 2020). Their 2023 study extended this framework through incremental two-scale algorithms coupling macro- and micro-contact problems (Rohan and Heczko, 2023). Later extensions considered fluid-saturated micropores with fluid–structure interaction and Stokes flow in connected porosity (Rohan and Heczko, 2026). The present work differs from these studies in its numerical emphasis. We do not aim to derive a new two-scale homogenisation theory for unilateral pore-scale contact. Instead, we focus on the microscale/RVE contact-resolution step required during updated-geometry property evaluation. In contrast to the semi-smooth Newton treatment of the local contact problem used in the studies above, the FE-discretised pore-wall contact problem is formulated here explicitly as an LCP and solved using a fast approximation strategy (FA-LCP). Unlike these authors, we further consider systems with multiple, randomly-distributed pores that can mechanically influence each other.

The primary contribution of this work is the FA-LCP method, a fast approximation for repeatedly solving the linear complementarity problem arising from evolving frictionless pore-wall contact. The method is integrated into a microscale FE workflow for updating the effective properties of porous RVEs. Specifically, the framework combines:

- updated-geometry FE simulations with segment-to-segment frictionless pore-wall contact;
- explicit reduction of the contact update to an LCP;
- the FA-LCP method for fast repeated contact resolution; and
- perturbation-based evaluation of incremental tangent stiffnesses and Biot coefficients on the updated configuration.

The method is benchmarked against Lemke and projected Gauss–Seidel solvers and applied to single-pore, multi-pore and complex randomly distributed pore geometries to quantify how progressive contact modifies anisotropic stiffness and poromechanical coupling.

2. Material model

In this section, the underlying system of mathematical governing equations for solid deformation and solid frictionless contact is introduced (with some of the more elaborate derivations postponed to Appendix A). Throughout this work, we consider a solid material, that surrounds an empty pore space, where the material properties of the solid are homogeneous and isotropic. We first consider the solid material as a body and introduce the appropriate state variables and powers, before defining the material model through the introduction of an energy potential for the bulk and for the surface. We then proceed to the spatial discretisation of the system using the finite element method, resulting in a semi-discretised system. Then, we treat the system as a representative volume element (RVE) of a porous material by introducing periodic boundary conditions and a perturbation method to compute the macroscopic properties of the system. (See Fig. 1.)

2.1. Continuous system

In Appendix A we systematically derive the equilibrium equations and state variables in the plane strain condition for a body Ω with boundary Γ, which we present here:

$$\begin{cases} \nabla \cdot \boldsymbol{\sigma} + \boldsymbol{f} = 0 & \text{in } \Omega, \\ \boldsymbol{\tau} = \boldsymbol{\sigma} \cdot \boldsymbol{n} & \text{on } \Gamma_{\mathcal{N}}, \\ \boldsymbol{u} = \boldsymbol{u}_D & \text{on } \Gamma_D, \\ r_{\mathrm{N}} = -(\boldsymbol{\sigma} \cdot \boldsymbol{n}) \cdot \boldsymbol{n} & \text{on } \Gamma \backslash \left(\Gamma_{\mathcal{N}} \cup \Gamma_D\right), \\ \Gamma_{\mathcal{N}} \cap \Gamma_D = \emptyset, \end{cases} \tag{1}$$

where $\boldsymbol{\sigma}$ is the usual Cauchy stress, $\boldsymbol{f}$ the body force, $\boldsymbol{n}$ is the unit normal vector on Γ, the $\mathcal{D}$ and $\mathcal{N}$ subscripts indicate the Dirichlet and Neumann boundary conditions respectively and r_{N} is the contact pressure. We further have the usual Cauchy strain $\boldsymbol{\epsilon}$ and the relative normal displacement between two surface elements u_{N}.

The free energy of the system gives us the laws that describes the reversible behaviour of the system. The free energy of the system Ψ is given by the sum of the free energy of the bulk material Ψ_e with the free energy of the surface Ψ_s:

$$\Psi = \int_{\Omega} \Psi_e(\boldsymbol{\epsilon}) \mathrm{d}V + \int_{\Gamma} \Psi_s(u_{\mathrm{N}}) \mathrm{d}S. \tag{2}$$

In this work we consider the bulk material to be purely linear elastic (and so the strain tensor is equivalent to the elastic strain tensor) and

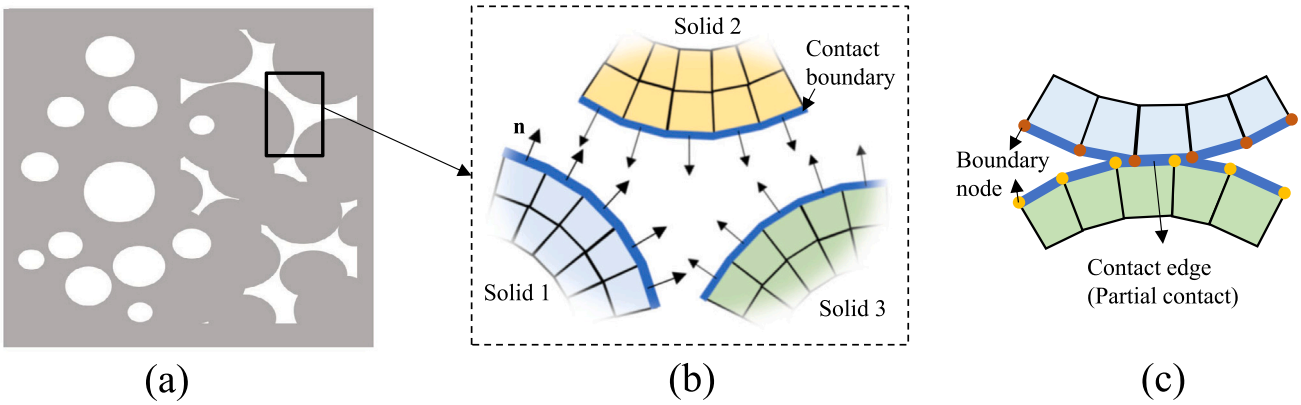


Fig. 1. (a) Microscopic porous media model with arbitrary pore structure (white for pore, grey for solid, incorporating (b) localised solid contact interactions (adapted from Batistić et al. (2022)) and (c) parallel solid contact configuration.

we may thus obtain the constitutive expression for the stresses with a classical specification of the bulk energy potential:

$$\Psi_e(\boldsymbol{\varepsilon}) = \frac{1}{2}\boldsymbol{\varepsilon} : \boldsymbol{D} : \boldsymbol{\varepsilon}, \tag{3}$$

$$\boldsymbol{\sigma}(\boldsymbol{\varepsilon}) = \frac{\partial \Psi_e(\boldsymbol{\varepsilon})}{\partial \boldsymbol{\varepsilon}} = \boldsymbol{D} : \boldsymbol{\varepsilon}, \tag{4}$$

where $\boldsymbol{D}$ is a fourth order elastic stiffness tensor with values determined by the Young's modulus E_s and Poisson's ratio ν_s of the solid material, and : indicates the double-contraction operation. For numerical implementations, we convert $\boldsymbol{D}$, $\boldsymbol{\varepsilon}$ and $\boldsymbol{\sigma}$ from tensors to matrices and vectors using the standard Voigt transformation, detailed in Appendix A.2.

In making this choice, we are assuming that the rotations and gradients of displacement that occur in the system are sufficiently small that a finite strain formulation is not required to obtain sufficient accuracy, and that plastic straining and damage do not occur. While a finite-strain formulation is strictly always more accurate, and while it is possible in that in areas of stress concentration plasticity and damage occur, the substantial numerical costs induced by the nonlinear bulk behaviour in either case would not be justified for our application, where we expect nonlinearity due to contact to dominate. We thus benefit from the numerical advantages of a linearised formulation in the bulk, and concentrate our theoretical and numerical developments on the contact behaviour. A purely linear elastic behaviour in the bulk also allows us to benefit from theoretical relationships derived by other authors linking the stiffness of the solid material with the overall stiffness parameters of the porous medium.

We obtain the contact pressure by an appropriate specification of the surface energy:

$$\Psi_s(u_\mathrm{N}) = \mathcal{I}_{\mathbb{R}_+}(u_\mathrm{N}), \tag{5}$$

$$-r_\mathrm{N} \in \partial_{u_\mathrm{N}} \Psi_s(u_\mathrm{N}), \tag{6}$$

where ∂_{u_N} indicates the subdifferential with respect to u_N and $\mathcal{I}_C$ is the indicator function of a convex set C. This constitutive specification has the effect of causing interface interpenetration ($u_\mathrm{N} < 0$) to be associated with infinite energy, and so to be forbidden. This is a standard formulation in nonsmooth mechanics when accounting for surfaces in order to ensure that the non-interpenetration constraint is respected (Frémond, 2002). Such potentials can in general be extended in order to consider adhesive, thermal or chemical effects, but here we restrict ourselves to consider only contact. As the subdifferential of the indicator set of the positive real numbers is the normal cone to the positive reals $\mathrm{N}_{\mathbb{R}_+}$, we may also write the contact pressure as

$$-r_\mathrm{N} \in \mathrm{N}_{\mathbb{R}_+}(u_\mathrm{N}), \tag{7}$$

which can in turn be further simplified as a complementarity relation enforcing impenetrability:

$$0 \le r_\mathrm{N} \perp u_\mathrm{N} \ge 0, \tag{8}$$

where $a \perp b$ symbol indicates that $a \cdot b = 0$, taken element-wise (*i.e.* in the case where the two quantities in complementarity are vectors, each pair of entries multiplies to zero).

2.2. Spatially discretised system

We consider now a finite-dimensional model of the system, where we discretise the model using the classical finite element method. We use Galerkin's method, so that the shape and weight functions are identical, and proceed in the standard fashion. While the method detailed in this paper can easily be generalised to higher order elements, here we further specialise in assuming that the discretisation is done using isoparametric linear triangle (T3) or quadrilateral (Q4) elements. These elements sufficiently balance accuracy and the size of the discrete system for our purposes.

Now, we denote our finite set of displacements $\boldsymbol{u} \in \mathbb{R}^n$, the external set of forces $\boldsymbol{F} \in \mathbb{R}^n$, and the structural stiffness matrix assembled in the standard way as $\boldsymbol{K} \in \mathbb{R}^{n\times n}$. This matrix will be symmetric and positive semi-definite. We consider also a finite set of contact points that are indexed by $\alpha \in [\![1, m]\!]$, and we assume that the local normal displacements at the contact (given by $\boldsymbol{u}_\mathrm{N} = \{\mathrm{col}(u_\mathrm{N}^\alpha), \alpha \in [\![1, m]\!]\}$) can be related to the global displacement with a linear relation given by

$$\boldsymbol{u}_\mathrm{N} = -\boldsymbol{B}_c\boldsymbol{u} + \boldsymbol{c}_\mathrm{N}, \tag{9}$$

where $\boldsymbol{B}_c \in \mathbb{R}^{m\times n}$ is a matrix that selects and interpolates the applicable degrees of freedom and $\boldsymbol{c}_\mathrm{N} \in \mathbb{R}_+^m$ is an initial gap function. In making this construction, we are assuming that the relative displacements are small enough to be linearised, an assumption justified by the fact that we only consider local normal displacements when points are already sufficiently close together to trigger "contact detection", a process we describe in detail in Section 3.3. We can also construct a diagonal matrix $\boldsymbol{S} \in \mathbb{R}^{m\times m}$ that contains the tributary area associated with each contact pressure. For the sake of notational simplicity, from here on we refer to the product of this tributary area with the contact pressure as the contact force $f_c^\alpha = S^\alpha r_\mathrm{N}^\alpha$, which can be converted to a column vector $\boldsymbol{f}_c$ in the same way as $\boldsymbol{u}_\mathrm{N}$. As the components of $\boldsymbol{S}$ are all positive and finite, and there is no interaction between the different terms, the complementarity relationship between r_N and u_N can be transferred to be between $\boldsymbol{f}_c$ and $\boldsymbol{u}_\mathrm{N}$. Finally, this gives the spatially-discretised system

$$\begin{cases} \boldsymbol{K}\boldsymbol{u} = \boldsymbol{F} - \boldsymbol{B}_c^\top \boldsymbol{f}_c, \\ \boldsymbol{u}_\mathrm{N} = -\boldsymbol{B}_c\boldsymbol{u} + \boldsymbol{c}_\mathrm{N}, \\ 0 \le \boldsymbol{u}_\mathrm{N} \perp \boldsymbol{f}_c \ge 0, \end{cases} \tag{10}$$

where the inequalities and complementarity are to be understood component-wise.

2.3. Periodic boundary conditions

In this work, the structure that we have discretised with the finite element is in fact the *microstructure* of the RVE of a porous material, in order to obtain its average macroscopic poromechanical properties. The Hill–Mandel principle of macro-homogeneity (Hill, 1963; Mandel, 1971) establishes a fundamental connection between macroscopic and microscopic deformation and stress. It states that the variation of work at a macroscopic point must equal the volume average of the microscopic work variation within the RVE. This principle also imposes constraints on the boundary conditions used in RVE simulations: either prescribed displacements, prescribed tractions, or periodic boundary conditions. Among these, periodic boundary conditions generally yield the most accurate homogenised properties (Nguyen et al., 2012; Terada et al., 2000; Kanit et al., 2003; Larsson et al., 2011). To impose periodic boundaries, displacement differences between corresponding boundaries are constrained. For the sake of clarity, the body Ω with boundary Γ that we have previously considered is merely the solid part of the microstructure. We can also treat the entire system (inclusive of the voids) as a body with a boundary for the purposes of homogenisation. To this end, we use the symbol V to refer to the RVE in its entirety, and its boundary as ∂V. While Ω is completely contained in V, only the Dirichlet and Neumann parts of Γ are necessarily contained in ∂V, and in general the "internal" boundaries on which the contact problem is solved will not belong to ∂V.

The RVE boundary ∂V is decomposed into two parts: a positive part ∂V^+ and a negative part ∂V^-, satisfying $\partial V^+ \cup \partial V^- = \partial V$, $\partial V^+ \cap \partial V^- = \emptyset$, with the outward normal $\boldsymbol{n}^+ = -\boldsymbol{n}^-$ at conjugate points $\boldsymbol{x}^+ \in \partial V^+$ and $\boldsymbol{x}^- \in \partial V^-$. This enforces periodicity of displacement fluctuations and antiperiodicity of tractions, as

$$\begin{cases} \boldsymbol{u}(\boldsymbol{x}^+) - \boldsymbol{u}(\boldsymbol{x}^-) = \bar{\boldsymbol{\varepsilon}}\,\Delta\boldsymbol{x}, & \forall \boldsymbol{x}^+ \in \partial V^+ \text{ and matching } \boldsymbol{x}^- \in \partial V^-, \\ \boldsymbol{\sigma}(\boldsymbol{x}^+)\cdot\boldsymbol{n}^+ = -\boldsymbol{\sigma}(\boldsymbol{x}^-)\cdot\boldsymbol{n}^-, & \forall\, \boldsymbol{x}^+ \in \partial V^+ \text{ and matching } \boldsymbol{x}^- \in \partial V^-. \end{cases} \tag{11}$$

where $\Delta\boldsymbol{x}$ denotes the periodic length of RVE and $\bar{\boldsymbol{\varepsilon}}$ is the macroscopic strain.

2.4. Perturbation method for macroscopic stiffness matrix

Here we use plane strain conditions to approximate a 3D material that is invariant and infinitely extended in the 2-direction. We want to determine the macroscopic incremental (tangent) effective properties of the RVE, so in two dimensions and under plane strain conditions in direction 2 the following constitutive relation holds:

$$\begin{bmatrix} \sigma_1 \\ \sigma_2 \\ \sigma_3 \\ \sigma_6 \end{bmatrix} = \begin{bmatrix} D_{11} & D_{12} & D_{13} & D_{16} \\ D_{21} & D_{22} & D_{23} & D_{26} \\ D_{31} & D_{32} & D_{33} & D_{36} \\ D_{61} & D_{62} & D_{63} & D_{66} \end{bmatrix} \begin{bmatrix} \varepsilon_1 \\ 0 \\ \varepsilon_3 \\ 2\varepsilon_6 \end{bmatrix}, \tag{12}$$

where σ_i and ε_i denote the stress and strain tensor components, respectively.

If the behaviour of the RVE is isotropic or transversely isotropic with respect to direction 2, the parameters D_{61}, D_{62}, D_{63} and D_{16}, D_{26} and D_{36} remain zero. Otherwise, these parameters acquire nonzero values, especially in shear displacement. To determine the components of $\boldsymbol{D}$, we apply the perturbation method (Charpin and Ehrlacher, 2014; Elishakoff et al., 1997), in which small perturbations are applied separately in horizontal, vertical, and shear displacements, and the corresponding stress variations $\delta\boldsymbol{\sigma}$ are computed for each perturbation direction. The average stress change is then obtained as

$$\delta\boldsymbol{\sigma} = \frac{\int_V \delta\boldsymbol{\sigma}_{\text{Gauss}}\,\mathrm{d}V}{\int_V \mathrm{d}V}, \tag{13}$$

where $\delta\boldsymbol{\sigma}$ represents the stress change of Gauss points in the volume V due to small displacement perturbations and $\boldsymbol{\sigma}_{\text{Gauss}}$ represents the stress state measured at a Gauss point.

In two dimensional plane strain conditions, the incremental tangent modulus and Poisson's ratio in the x_2-direction are functions of the mechanical properties of the solid matrix and porosity n (Charpin and Ehrlacher, 2014; Nguyen et al., 2012; Nemat-Nasser and Hori, 1998), *i.e.*

$$E_2 = (1-n)E_s, \tag{14}$$

$$\nu_{21} = \nu_{23} = \nu_s. \tag{15}$$

The Young's modulus in the x_1- and x_3-directions, E_1 and E_3, shear modulus G_{13} and Poisson's ratio ν_{13} can be expressed using the calculated stiffness parameters D_{ij} using results from Charpin and Ehrlacher (2014), which we present in Appendix A.3.

In addition to the classical elastic properties of the homogenised material, we are also interested in obtaining an estimate of the Biot coefficients in each direction of the material, which are given by Tan and Konietzky (2014):

$$b_1 = 1 - \frac{D_{11}+D_{12}+D_{13}}{3K_s}, \tag{16}$$

$$b_2 = 1 - \frac{D_{12}+D_{22}+D_{23}}{3K_s}, \tag{17}$$

$$b_3 = 1 - \frac{D_{13}+D_{23}+D_{33}}{3K_s}, \tag{18}$$

where K_s is the bulk modulus of the solid phase, *i.e.* $K_s = \frac{E_s}{3(1-2\nu_s)}$. Note that the Biot coefficients are inferred from the homogenised stiffness matrix and the solid-phase bulk modulus, and no explicit pore-fluid flow or pore-pressure problem is solved. The reported coefficients should therefore be interpreted as stiffness-derived estimates under the assumptions underlying these relations.

3. Numerical solution

Having obtained an analytical description of the spatially-discretised but time-continuous system, we now turn to the load-stepping discretised system and its numerical resolution. We first describe the pre-processing of the system that allows the spatially discrete system to be imported and correctly interpreted by the numerical simulator. We then describe the load-stepping scheme and the contact detection and classification algorithm, leading to the formulation of the fully discretised system as a linear complementarity problem. We prove that this problem has solutions, and provide the condition under which the solution is unique. The central computational problem in solid contact analysis lies in the presence of two unknowns (u_{N} and f_c) where at least one variable must vanish at each contact point. To overcome these limitations, we then describe the algorithm developed to provide a fast approximation of the solution of this system. Finally, we describe the numerical resolution of the perturbation problem and discuss the consistency of the numerical model with the theoretical formulation. The entire numerical solution process is integrated into an in-house simulator, with the iterative workflow illustrated in Fig. 2. The simulation codes, written in Fortran 90, were run on Windows 10/11 and compiled with the Intel Fortran Compiler 2024.2 (IFORT, oneAPI HPC Toolkit).

3.1. Pre-processing

In order to efficiently carry out the simulations, we first pre-process the system. The mesh is generated either using the commercial Gambit software or with the Python toolbox Nanomesh (Smeets et al., 2022) and then converted to Gambit format with an in-house developed script. The generated Gambit neutral files are directly read in by our code. However, nothing about our method requires use of this particular meshing software, so any suitable software that produces conforming meshes can easily be substituted.

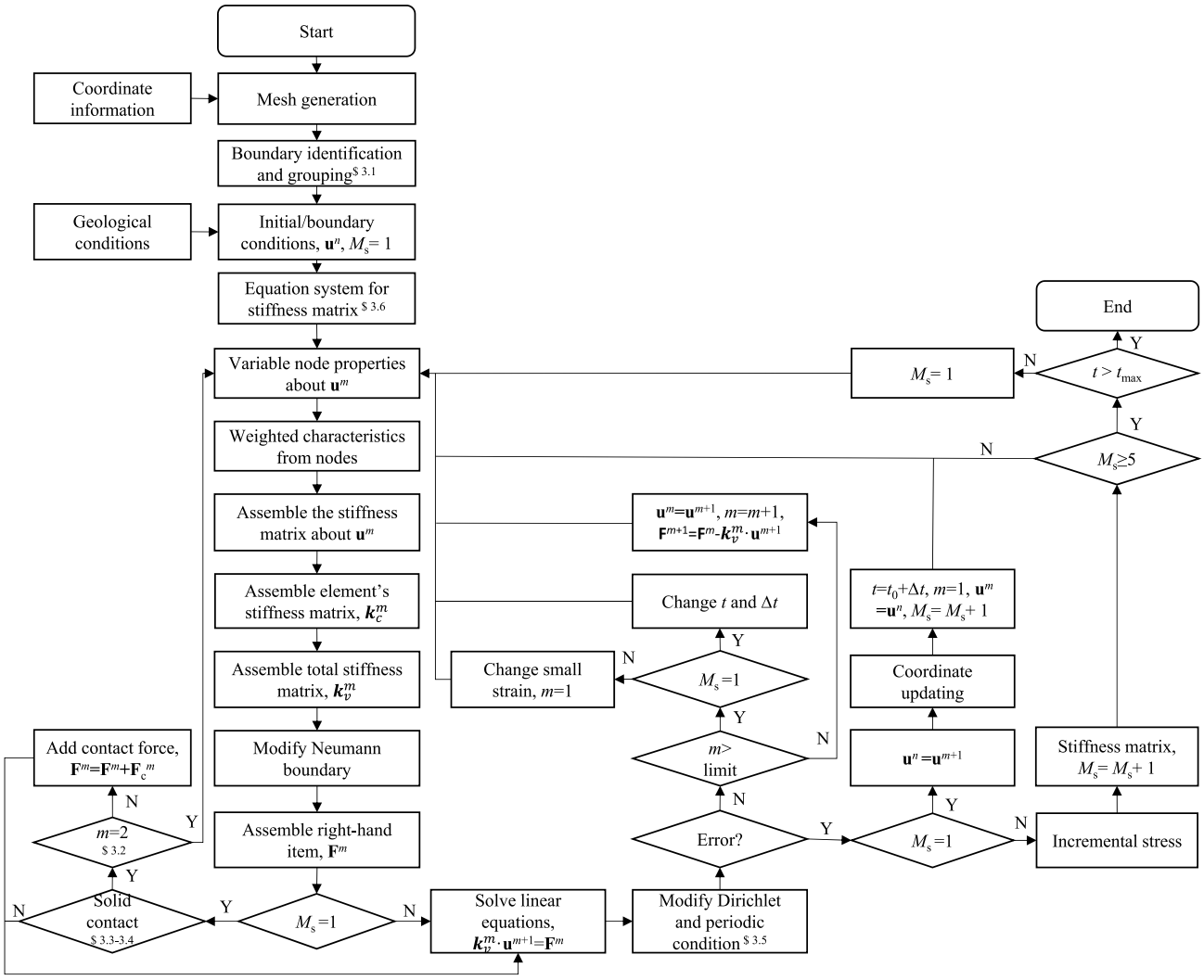


Fig. 2. FEM workflow for micromechanical deformation analysis with consideration of solid contact resolution and automated stiffness matrix updating.

Then, we analyse the system to identify which elements lie on the pore surface and thus are able to be in contact with each other. We loop through each edge in the mesh, and if that edge is present only in one element, we identify it as a possible contact surface. Then, for all of the contact surfaces, we construct an adjacency list that records which other surface nodes it is directly connected to by a boundary edge. Finally, all nodes that are directly connected through boundary edges are assigned to a contact group, and members of each group can only (potentially) be in contact with other members of the same group. This ensures that no computational resources are expended checking contact conditions on pairs of contact surfaces that belong to different pores.

Finally, the structural stiffness matrix $\boldsymbol{K}$ is generated by assembling the element stiffness matrices following the standard finite element methodology. The structural stiffness matrix is then modified in the standard way to impose the Dirichlet boundary conditions (making the matrix positive definite), and we may obtain the final LCP by calculating the modified compliance matrix by inversion of the modified stiffness matrix. In practice we do not actually invert the matrix and instead we obtain the LU decomposition, and each inverted stiffness matrix $\boldsymbol{K}^{-1}$ (or any other matrix inverse) that appears below should be understood to actually be the LU decomposition acting on the appropriate terms.

3.2. Initial iteration

The problem is formulated in a quasi-static setting and solved incrementally using a load-stepping procedure. The increment counter is denoted by $\mathsf{k} \in \mathbb{N}$, and the corresponding pseudo-time is denoted by t_{k}. The displacement field and external force vector at step k are denoted by $\boldsymbol{u}_{\mathsf{k}}$ and $\boldsymbol{F}_{\mathsf{k}}$, respectively. A backward-Euler-type incremental update is employed in the sense of load progression, that is

$$\int_{t_{\mathsf{k}}}^{t_{\mathsf{k}+1}} a(t)\mathrm{d}t \approx \Delta t a(t_{\mathsf{k}+1}), \tag{19}$$

where $a(t)$ represents some arbitrary variable. We begin the process of updating the system by updating the external force vector $\boldsymbol{F}_{\mathsf{k}+1}$, using the user-defined load increments. Any force contributions of elements lying on Neumann boundaries are obtained, and then all of the element contributions are assembled into the global force vector. The force vector is then modified in the standard way to impose the Dirichlet boundary conditions at $t_{\mathsf{k}+1}$. We then calculate the trial displacement assuming no contacts, which gives the first internal iterate of the system:

$$\boldsymbol{u}^1 = \boldsymbol{K}^{-1}\boldsymbol{F}_{\mathsf{k}+1}, \tag{20}$$

From this point, we may pass to the detection and classification of contacts.

Algorithm 1 Contact detection algorithm with displacement scaling and boundary-surface verification

Require: contact groups, $\boldsymbol{x}^0$, $\boldsymbol{u}^1$, total scaling steps n
for group $\in$ contact groups **do** ▷ Check each possible contact group separately
for Ele1 $\in$ group **do**
for Ele2 $\in$ group\elements<Ele1 **do** ▷ Check each element pair only once
contactEle12 $\leftarrow$ FALSE ▷ Assume no contact
for $i = \mathsf{n}$ to 1 **do** ▷ Progressive displacement scaling
$\bar{\boldsymbol{u}}_i^1 \leftarrow \frac{i}{n}\boldsymbol{u}^1$
for node1 $\in$ contact surface of Ele1 **do**
for node2 $\in$ contact surface of Ele2 **do** ▷ Check each node pair
$\boldsymbol{u}_{\mathrm{N,node1node2}} \leftarrow (\boldsymbol{x}^0_{\mathrm{node1}} + \bar{\boldsymbol{u}}^1_{i,\mathrm{node1}}) - (\boldsymbol{x}^0_{\mathrm{node2}} + \bar{\boldsymbol{u}}^1_{i,\mathrm{node2}})$
if $\boldsymbol{u}_{\mathrm{N}} \leq 0$ **then**
in12 $\leftarrow$ any part of Ele1 boundary lies inside Ele2
in21 $\leftarrow$ any part of Ele2 boundary lies inside Ele1
if in12 = TRUE **and** in21 = TRUE **then**
contactEle12 $\leftarrow$ TRUE ▷ Contact detected
break
end if
end if
end for
if contactEle12 = TRUE **then**
break
end if
end for
if contactEle12 = TRUE **then**
break
end if
end for
end for
end for
end for
return List of element pairs for which contactEle12 is TRUE

3.3. Contact detection and classification

3.3.1. Contact detection

Once the first internal iterate has been obtained, we use this virtual geometry as the system configuration on which the contact detection operates. We implement Algorithm 1 to check for the presence of contacts.

This algorithm loops through the elements in each contact group, then loops again through the elements with a higher element number in the same contact group (ensuring that a given pair of elements is checked only once), then checks each pair of nodes in these elements (in12 and in21) to determine if the "contactEle12" (contact between Ele1 and Ele2) is satisfied, when the normal gap function (9) is negative. However, during the detection of contacts, only potential boundary elements are assessed, excluding internal elements. Excessive displacements may cause over-penetration of contact boundaries, as shown in Fig. 3(a). In this example, Element 1 undergoes calculated deformation in the initial step and penetrates through Boundary Element 2 to contact Internal Element 3, which is not evaluated by the detection routine. In reality, Element 1 should first establish contact with Element 2. Consequently, some potential contact pairs may be missed. To mitigate against this, geometric overlap is re-evaluated by progressively scaling displacements from the updated virtual configuration back to the initial state, given by

$$\bar{\boldsymbol{u}}_i^1 = \frac{i}{\mathsf{n}}\boldsymbol{u}^1, \tag{21}$$

where $i \in \{1, 2, \ldots, \mathsf{n}\}$ and n indicates the total scaling steps. This operation is applied to all element pairs for which contact is not detected in the initial virtual geometry. Then, for each i considered, contacts are checked again. This operation is repeated until all element pairs in the same boundary group have been checked, and then repeated for each boundary group until the contacts are fully characterised. Contact groups are identified if overlap occurs at any scaled configuration.

Additionally, even if two boundary elements are found to overlap, direct contact is only confirmed if their surfaces actually interact, as shown in Fig. 3(b). In this case, Element 1 overlaps with Element 3 by passing through the intermediate Boundary Element 2. However, the true contact should occur between Element 1 and Element 2, not Element 3. Therefore, contact is considered established when parts of the boundary surfaces of both interacting elements are simultaneously located within the contact region, indicating a partial overlap. If the apparent overlap involves only one element's boundary, the pair is treated as cross contact and non-contacting. If no contacts are detected for all values of i, there are no contacts in that loading step and $\boldsymbol{u}^1$ is accepted as the solution. If contacts are detected, we then proceed to Section 3.3.2. In such cases, the loading step Δt is adaptively reduced to enhance the resolution of incremental strain, stress, and displacement changes, allowing accurate identification of the transition from non-contact to contact states while minimising numerical errors. Therefore, different initial loading steps are assigned to the pre-contact and post-contact phases. Before contact occurs, a relatively large initial loading step is used to accelerate convergence. Once the first contact is detected, the loading step is automatically reduced according to user-defined parameters (by default, it is reduced to one-tenth of the initial value). This adaptive reduction ensures smooth transition between loading stages and prevents over-penetration. After the first contact is established, the maximum allowable loading step is also reset, providing tighter control on subsequent deformation increments.

3.3.2. Contact classification

We apply a surface-to-surface contact scheme where we assume that the contacting surfaces of two elements are parallel at the moment of contact, but are not necessarily aligned node-to-node. We assume a

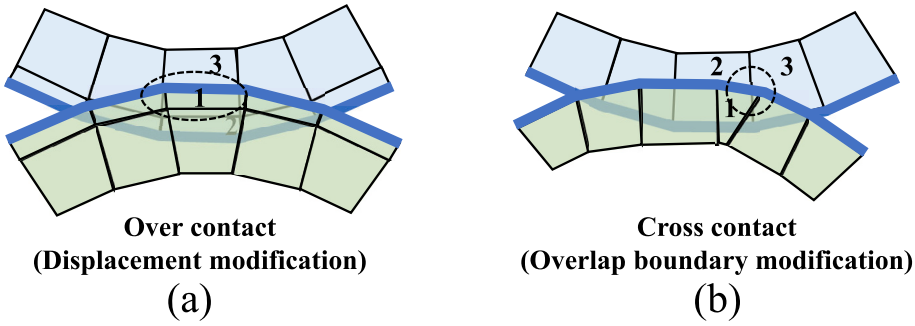


Fig. 3. Displacement modification for (a) over contact and (b) overlap boundary modification for cross contact in solid contact group recognition. Blue lines describe the contact edges. Elements 1 and 2 represent the physically consistent contact boundary elements, while element 3 denotes a falsely identified contact element. The simulation results indicate an incorrect detection of contact between elements 1 and 3, whereas the physically correct contact should occur between elements 1 and 2.

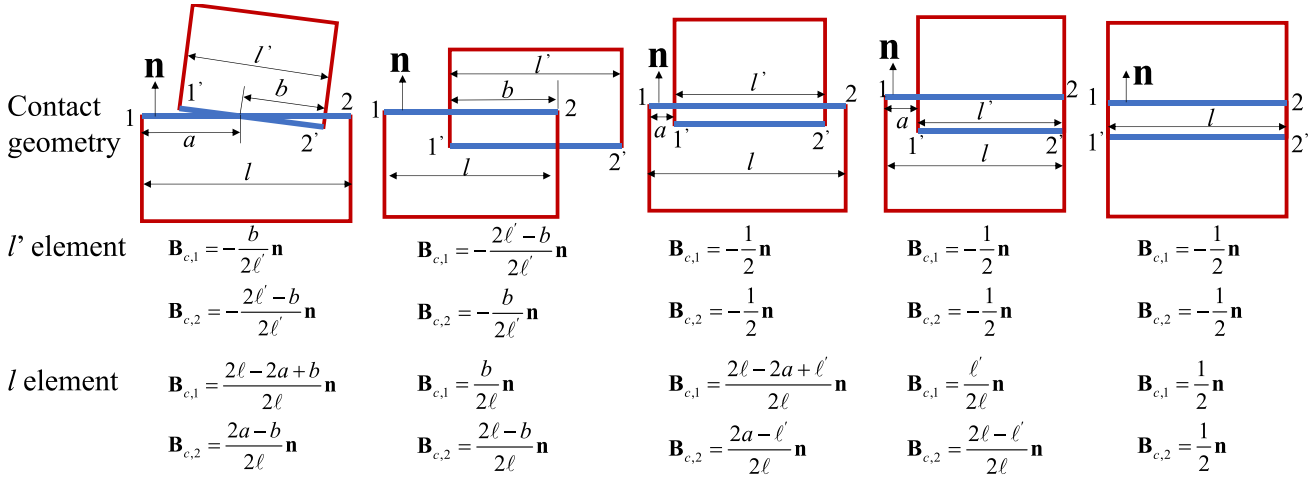


Fig. 4. The contact selection and interpolation matrix construction rules. Blue lines describe the contact edges. $\boldsymbol{B}_{c,1}$ and $\boldsymbol{B}_{c,2}$ should be understood to refer to the entries that correspond to the appropriate row for the given contact pair, and to the appropriate columns for the node under consideration.

constant distribution of pressure along the contacting surfaces and apply a set of characterisation rules to appropriately allocate the contact forces to the nodes in the problem. For a pair of contacting elements identified by Algorithm 1, which possess contacting surfaces of length ℓ and ℓ' with $\ell' \leq \ell$, the length of the overlapping part of the surfaces is given by b and the distance from the node of the contacting surface with length ℓ to the edge of the overlapping region is given by a, as shown in the subfigures in Fig. 4. The surface normals and the initial gap functions are evaluated from the geometry of the previous loading step. The element associated with the contacting surface of length ℓ is assigned the outward-pointing normal vector $\boldsymbol{n}$, while its counterpart with surface length ℓ' is assigned the opposite normal vector $-\boldsymbol{n}$. During the loading process, perfectly parallel contact surfaces cannot be maintained. The contact normal is therefore defined as the average normal of the two interacting contact surfaces. We construct a contact interpolation and selection matrix $\boldsymbol{B}_c \in \mathbb{R}^{m\times n}$ where m is the number of element contact pairs identified by Algorithm 1. We consider one contact problem per element contact pair. The contact type is determined based on the number of boundary nodes of one element that lie inside the other element, and the contact selection and interpolation matrix is constructed accordingly, as summarised in Fig. 4.

The $\boldsymbol{B}_{c,1}$ and $\boldsymbol{B}_{c,2}$ entries of the ℓ element and ℓ' element are then assembled into the appropriate row of the contact selection and interpolation matrix $\boldsymbol{B}_c$. The remaining entries in that row are set to zero. The normal contact distance vector $\boldsymbol{c}_{\mathrm{N,k}}$ at loading step k is then obtained by taking the average normal distance of the corresponding pairs of nodes belonging to the contacting surfaces of each contact pair. The resulting contact constraint is evaluated against the prescribed contact condition, and the contact force is iteratively adjusted until the constraint is satisfied within the specified tolerance. If convergence cannot be achieved for the current loading increment, the increment is further reduced to improve the accuracy and stability of the contact solution.

3.4. Contact problem formulation

Having completed the contact detection and classification step, we have all of the necessary information to construct the contact problem at loading step k + 1. The normal contact distance is given by

$$\boldsymbol{u}_{\mathrm{N,k+1}} = -\boldsymbol{B}_c\boldsymbol{u}_{\mathrm{k+1}} + \boldsymbol{c}_{\mathrm{N,k}}. \tag{22}$$

The global discrete force equilibrium equation is given by

$$\boldsymbol{K}\boldsymbol{u}_{\mathrm{k+1}} = \boldsymbol{F}_{\mathrm{k+1}} - \boldsymbol{B}_c^{\mathrm{T}}\boldsymbol{f}_{c,\mathrm{k+1}}, \tag{23}$$

where $\boldsymbol{f}_{c,\mathrm{k+1}}$ is the contact force between a pair of contacting elements, and the contact distance and contact force respect the linear complementarity condition

$$0 \leq \boldsymbol{u}_{\mathrm{N,k+1}} \perp \boldsymbol{f}_{c,\mathrm{k+1}} \geq 0, \tag{24}$$

where the complementarity should be understood to act pair-wise (that is the ith entry of $\boldsymbol{u}_{\mathrm{N,k+1}}$ is in complementarity with the ith entry of $\boldsymbol{f}_{c,\mathrm{k+1}}$). Straightforward re-arrangement and combination of (22), (23)

and (24) gives the system

$$\begin{cases} \boldsymbol{u}_{\mathrm{N},k+1} = \boldsymbol{B}_c \boldsymbol{K}^{-1} \boldsymbol{B}_c^{\top} \boldsymbol{f}_{c,k+1} - \boldsymbol{B}_c \boldsymbol{K}^{-1} \boldsymbol{F}_{k+1} + \boldsymbol{c}_{\mathrm{N},k}, \\ 0 \leq \boldsymbol{u}_{\mathrm{N},k+1} \perp \boldsymbol{f}_{c,k+1} \geq 0. \end{cases} \tag{25}$$

For reasons of clarity and compactness we denote the quantity $\boldsymbol{B}_c \boldsymbol{K}^{-1} \boldsymbol{B}_c^{\top}$ as $\boldsymbol{W}$, and the quantity $-\boldsymbol{B}_c \boldsymbol{K}^{-1} \boldsymbol{F}_{k+1} + \boldsymbol{c}_{\mathrm{N},k}$ as $\boldsymbol{q}$. The matrix $\boldsymbol{W}$ is often referred to in contact mechanics as the Delassus matrix (Brogliato, 2016). We refer to (25) compactly as LCP($\boldsymbol{W}, \boldsymbol{q}$).

3.4.1. Well-posedness of the linear complementarity problem

Lemma 1. *The LCP($\boldsymbol{W}, \boldsymbol{q}$) possesses at least one solution for physically admissible $c_{\mathrm{N},k} \geq 0$.*

Proof. First, we must show that $\boldsymbol{W}$ is at least positive semi-definite. We have that the structural stiffness matrix $\boldsymbol{K}$ is symmetric by construction, and the modifications made to impose the Dirichlet boundary conditions change it from positive semi-definite to positive definite, without modifying the symmetry, and this property necessarily holds for its inverse. Any matrix product of the form $\boldsymbol{A}\boldsymbol{B}\boldsymbol{A}^{\top}$ is at least positive semi-definite if $\boldsymbol{B}$ is positive definite. As this is exactly the structure of $\boldsymbol{W}$ with respect to $\boldsymbol{B}_c$ and $\boldsymbol{K}^{-1}$, we have that $\boldsymbol{W}$ is at least positive semi-definite.

Next, we must show that the LCP($\boldsymbol{W}, \boldsymbol{q}$) is feasible, with the feasibility conditions being $\boldsymbol{W}\boldsymbol{f}_{c,k+1} + \boldsymbol{q} \geq 0$ and $\boldsymbol{f}_{c,k+1} \geq 0$. Suppose that LCP($\boldsymbol{W}, \boldsymbol{q}$) is infeasible. Then, by Farkas' lemma, there exists a vector $\boldsymbol{v} \geq 0$ such that $\boldsymbol{W}^{\top}\boldsymbol{v} \leq 0$ and $\boldsymbol{q}^{\top}\boldsymbol{v} < 0$. As $\boldsymbol{W}$ is at least positive semi-definite, and is symmetric by construction, any $\boldsymbol{v} \geq 0$ with $\boldsymbol{W}^{\top}\boldsymbol{v} \leq 0$ must be in the kernel $\ker(\boldsymbol{W})$, as $0 \leq \boldsymbol{v}^{\top}\boldsymbol{W}\boldsymbol{v} = \boldsymbol{v}^{\top}(\boldsymbol{W}\boldsymbol{v}) \leq 0$ because $\boldsymbol{v} \geq 0$ and $\boldsymbol{W}\boldsymbol{v} \leq 0$ component-wise can only be satisfied by $\boldsymbol{v}^{\top}\boldsymbol{W}\boldsymbol{v} = 0$, and the positive semi-definiteness of $\boldsymbol{W} \implies \boldsymbol{W}\boldsymbol{v} = 0$. From the construction of $\boldsymbol{W} = \boldsymbol{B}_c \boldsymbol{K}^{-1} \boldsymbol{B}_c^{\top}$ with $\boldsymbol{K}^{-1}$ positive definite, we have the direct implication that $\ker(\boldsymbol{W}) = \ker(\boldsymbol{B}_c^{\top})$. Now, consider $\boldsymbol{q}^{\top}\boldsymbol{v}$. We have that

$$\begin{aligned} \boldsymbol{q}^{\top}\boldsymbol{v} &= \left(-\boldsymbol{B}_c \boldsymbol{K}^{-1} \boldsymbol{F}_{k+1} + \boldsymbol{c}_{\mathrm{N},k}\right)^{\top} \boldsymbol{v}, \\ &= -\boldsymbol{F}_{k+1}^{\top} \boldsymbol{K}^{-1} \boldsymbol{B}_c^{\top} \boldsymbol{v} + \boldsymbol{c}_{\mathrm{N},k}^{\top} \boldsymbol{v}, \\ &= \boldsymbol{c}_{\mathrm{N},k}^{\top} \boldsymbol{v} \geq 0, \end{aligned} \tag{26}$$

where we used our previous result that the first term of the expansion is orthogonal, and by assumption $\boldsymbol{c}_{\mathrm{N},k}$ and $\boldsymbol{v}$ are component-wise non-negative. Hence, the condition $\boldsymbol{q}^{\top}\boldsymbol{v} < 0$ cannot be fulfilled, and therefore the supposition that LCP($\boldsymbol{W}, \boldsymbol{q}$) is infeasible is false, and the LCP is feasible.

From Theorem 3.1.2 in Cottle et al. (2009), if the LCP($\boldsymbol{W}, \boldsymbol{q}$) with a positive semi-definite $\boldsymbol{W}$ is feasible, it is also solvable. We have shown $\boldsymbol{W}$ is positive semi-definite and the feasibility of LCP($\boldsymbol{W}, \boldsymbol{q}$), hence a solution exists. □

Lemma 2. *The LCP($\boldsymbol{W}, \boldsymbol{q}$) has a unique solution in $\boldsymbol{u}_{\mathrm{N},k+1}$, but we cannot determine the uniqueness of the solution for individual entries in $\boldsymbol{f}_{c,k+1}$.*

Proof. We denote the set of solutions of LCP($\boldsymbol{W}, \boldsymbol{q}$) by SOL($\boldsymbol{W}, \boldsymbol{q}$), which by Theorem 3.1.7 of Cottle et al. (2009) is a polyhedral set when $\boldsymbol{W}$ is positive semi-definite. This solution set is explicitly given by

$$\begin{aligned} \mathrm{SOL}(\boldsymbol{W}, \boldsymbol{q}) = \Big\{ \boldsymbol{f}_{c,k+1} \Big| & \boldsymbol{f}_{c,k+1} \geq 0, \boldsymbol{W}\boldsymbol{f}_{c,k+1} + \boldsymbol{q} \geq 0, \\ & \boldsymbol{q}^{\top}(\boldsymbol{f}_{c,k+1} - \bar{\boldsymbol{f}}_{c,k+1}) = 0, \\ & \boldsymbol{W}(\boldsymbol{f}_{c,k+1} - \bar{\boldsymbol{f}}_{c,k+1}) = 0 \Big\}, \end{aligned} \tag{27}$$

where $\bar{\boldsymbol{f}}_{c,k+1}$ is an arbitrary solution. The final condition $\boldsymbol{W}(\boldsymbol{f}_{c,k+1} - \bar{\boldsymbol{f}}_{c,k+1}) = 0$ gives us $\boldsymbol{u}_{\mathrm{N},k+1} - \bar{\boldsymbol{u}}_{\mathrm{N},k+1} = \boldsymbol{W}(\boldsymbol{f}_{c,k+1} - \bar{\boldsymbol{f}}_{c,k+1}) = 0$ from which we can immediately conclude that $\boldsymbol{u}_{\mathrm{N},k+1}$ is unique. We also conclude that $\boldsymbol{f}_{c,k+1} - \bar{\boldsymbol{f}}_{c,k+1}$ is in the kernel of $\boldsymbol{W}$ and thus also of $\boldsymbol{B}_c^{\top}$, so we obtain that $\boldsymbol{B}_c^{\top}(\boldsymbol{f}_{c,k+1} - \bar{\boldsymbol{f}}_{c,k+1}) = 0$. Then, from the second condition of (27), we have

$$\left(-\boldsymbol{B}_c \boldsymbol{K}^{-1} \boldsymbol{F}_{k+1} + \boldsymbol{c}_{\mathrm{N},k}\right)^{\top} (\boldsymbol{f}_{c,k+1} - \bar{\boldsymbol{f}}_{c,k+1}) = 0. \tag{28}$$

Then we can rearrange this to

$$\begin{aligned} &\left(-\boldsymbol{K}^{-1} \boldsymbol{F}_{k+1}\right)^{\top} \boldsymbol{B}_c^{\top} \left(\boldsymbol{f}_{c,k+1} - \overline{\boldsymbol{f}}_{c,k+1}\right) \\ &\quad + \boldsymbol{c}_{N,k}^{\top} \left(\boldsymbol{f}_{c,k+1} - \overline{\boldsymbol{f}}_{c,k+1}\right) = 0. \end{aligned} \tag{29}$$

The first member of the left hand side is zero as $\boldsymbol{B}_c^{\top}(\boldsymbol{f}_{c,k+1} - \bar{\boldsymbol{f}}_{c,k+1}) = 0$. We are left with $\boldsymbol{c}_{\mathrm{N},k}^{\top}(\boldsymbol{f}_{c,k+1} - \bar{\boldsymbol{f}}_{c,k+1}) = 0$, from which no conclusion as to uniqueness of the individual entries can be drawn *a priori*. □

The lack of uniqueness of contact forces is a well-known feature of quasi-static contact mechanics (Brogliato, 2016), however it is not of particular concern to us as the contact normal displacements $\boldsymbol{u}_{\mathrm{N}}$ are the primary variable that we are concerned with for the purposes of our numerical homogenisation method. It is also worth noting that the condition $\boldsymbol{B}_c^{\top}(\boldsymbol{f}_{c,k+1} - \bar{\boldsymbol{f}}_{c,k+1}) = 0$ does imply that the "assembled" contact force vector $\boldsymbol{B}c^{\top}\boldsymbol{f}_{c,k+1}$ is unique, and in the case where $\boldsymbol{B}_c$ has full rank, $\boldsymbol{W}$ is positive definite and the force solution is indeed unique. However, this condition typically does not hold, and it is impossible to know *a priori* if this condition will be obtained at any point in a given simulation, as $\boldsymbol{B}_c$ typically changes both its dimensions and the values of individual entries during a simulation.

3.4.2. Numerical resolution of the linear complementarity problem

In general, there are many solution methods to resolve linear complementarity problems. Of particular note is Lemke's algorithm (Lemke and Howson, 1964; Lemke, 1965), which is guaranteed to find a solution should one exist (and we have demonstrated that solutions always exist for our system, so this algorithm will always find one). However, this algorithm (and other classic algorithms for the linear complementarity problem such as the projected Gauss–Seidel method (Jourdan et al., 1998)) are generally quite slow. The FA-LCP method presented in this paper is developed with an eye towards its future implementation in the context of multiscale finite element simulations (simulations where the classical constitutive law at a quadrature point of the "macro-scale" finite element model is replaced with the homogenised results of a simulation conducted at the "micro-scale"), wherein many thousands of finite element simulations need to be completed rapidly to obtain macro-scale results in a timely manner. As such, we present a fast method of approximating the solution of the linear complementarity problem that gives us tolerable accuracy at sufficient speed.

Using the displacement field obtained from the initial iteration (Section 3.2), the proposed iterative contact algorithm first identifies all active contact pairs and assembles (25) as a linear system before iteratively solving the system and updating the contact constraints. The overall computational workflow is illustrated in Fig. 2. Within this workflow, the assembled linear system is solved using the procedure detailed in Algorithm 2. After initialising the system, the algorithm first solves the linear form of (25), that is solved to obtain the values of $\boldsymbol{f}_{c,k+1}$ coherent with $\boldsymbol{u}_{\mathrm{N},k+1} = 0$. This is achieved by solving a sequence of linear systems, rather than explicitly forming $\boldsymbol{K}^{-1}$, which would be computationally prohibitive and numerically unstable for large-scale problems. At each iteration, the linearised equations are solved using an LU decomposition (specifically the Pardiso parallel sparse direct solver (Schenk and Gärtner, 2004)). Then, as this can potentially result in negative $\boldsymbol{f}_{c,k+1}$ (that is to say, tensile contact forces that do not respect the complementarity condition), the subsequent line projects the contact forces back onto the positive orthant. At the same time, the contact displacements are updated iteratively to satisfy the complementarity condition. Using these results, a new value of the global contact force for each node $\boldsymbol{B}_c\boldsymbol{f}_{c,k+1}$ is obtained, from which the updated global displacements are calculated based on (10) and

Algorithm 2 Iterative solution procedure for the contact problem.

Require: $\boldsymbol{K}$, $\boldsymbol{B}_c$, $\boldsymbol{F}_{\mathrm{k+1}}$, $\boldsymbol{c}_{\mathrm{N,k}}$, tolerance $\eta = 10^{-7}$, maximum iterations $j_{\max} = 10$
  $\boldsymbol{u}^{j}_{\mathrm{k+1}} \leftarrow \boldsymbol{0}$, $\boldsymbol{f}_{c,\mathrm{k+1}} \leftarrow \boldsymbol{0}$, $j \leftarrow 0$
  Detect active contact pairs N_c by Algorithm 1 based on $\boldsymbol{u}^1$
  repeat
    $\boldsymbol{Y}_f \leftarrow \boldsymbol{K}\boldsymbol{Y}_f = \boldsymbol{F}_{\mathrm{k+1}} - \boldsymbol{B}_c^{\top}\boldsymbol{f}_{c,\mathrm{k+1}}$ ▷ Solved with LU factorisation
    $\boldsymbol{c}_f = \boldsymbol{B}_c\boldsymbol{Y}_f$
    $\boldsymbol{Y} \leftarrow \boldsymbol{K}\boldsymbol{Y} = \boldsymbol{B}_c^{\top}$ ▷ Solved with LU factorisation
    $\boldsymbol{W} = \boldsymbol{B}_c\boldsymbol{Y}$
    $\boldsymbol{f}_c^{j} \leftarrow \boldsymbol{W}\boldsymbol{f}_c^{j} = \boldsymbol{c}_f - \boldsymbol{c}_{\mathrm{N}}$ ▷ Determine contact force increment
    $\boldsymbol{f}_c^{j} \leftarrow \max(0, \boldsymbol{f}_c^{j})$ ▷ Enforce non-negative contact forces
    $\boldsymbol{u}^{j}_{\mathrm{k+1}} \leftarrow \boldsymbol{K}\boldsymbol{u}^{j}_{\mathrm{k+1}} = \boldsymbol{B}_c^{\top}\boldsymbol{f}_c^{j}$ ▷ Compute displacement correction
    $\boldsymbol{f}_{c,\mathrm{k+1}} \leftarrow \boldsymbol{f}_{c,\mathrm{k+1}} + \boldsymbol{f}_c^{j}$ ▷ Update accumulated contact force
    $\boldsymbol{u}_{\mathrm{k+1}} \leftarrow \boldsymbol{u}_{\mathrm{k+1}} + \boldsymbol{u}^{j}_{\mathrm{k+1}}$ ▷ Update displacement field
    $e \leftarrow \max_j |u^{j}_{\mathrm{k+1}}|$
    if $e < \eta$ **then**
      break ▷ Convergence condition
    end if
    Detect the active contact pairs based on $\boldsymbol{u}_{\mathrm{k+1}}$
    $j \leftarrow j + 1$
  until the active contact set is unchanged or $j = j_{\max}$ ▷ Convergence condition
  if $j = j_{\max}$ **then**
    $\Delta t \leftarrow \Delta t/2$ and restart the current time step
  end if
    return $\boldsymbol{f}_{c,\mathrm{k+1}}$, $\boldsymbol{u}_{\mathrm{k+1}}$

subsequently used for contact re-detection. This procedure is repeated until either (i) the active contact set remains unchanged between two successive iterations (including no contact in the initial iteration) or (ii) the maximum displacement correction from the current iteration step is less than 10^{-7} mm. If convergence is not achieved within the prescribed maximum number of contact iterations (10 in the present study), the current time step is reduced by half, and the contact iteration is restarted.

The underlying logic of the method is that the solution of the full LCP that is identified with the contact detection from Algorithm 1 can be well-approximated by the solution of a smaller LCP, constructed from the elements that remain in contact after the first step (and this LCP can in turn be well-approximated by another smaller LCP, and so on). This relies on a heuristic that contact points that have been identified as not in contact are very unlikely to be brought back into contact by subsequent iterations, as any subsequent correction is likely to be smaller in magnitude than the initial one. The inherent structure of the problem given by the geometry, constitutive law and finite element discretisation also causes the individual contact problems to be coupled in a way favourable to this heuristic (as the contact force generated at one contact point can effectively act on other contact points through the stiffness matrix to stop them coming into contact). We emphasise that this underlying heuristic is not a general solution technique for LCPs (*i.e.* it may fail completely on LCPs related to non-mechanical problems or mechanical problems with a less favourable structure), and it does not have any analytical guarantees that it will converge towards the solution of the full LCP. Hence, we refer to it as an approximation method, rather than a solution method.

3.5. Periodic problem

In order to enforce periodic boundary conditions, the RVE boundary must be discretised using a mapped node formulation (Nguyen et al., 2012). Each mapped node pair consists of a node on the negative boundary ∂V^- and its counterpart on the positive boundary ∂V^+. Consequently, the displacement vector $\boldsymbol{u}_{\mathrm{k+1}}$ in (23) is partitioned into three components (Nguyen et al., 2012): internal displacements $\boldsymbol{u}^{\mathrm{k+1}}_{\mathrm{int}}$, positive boundary displacements $\boldsymbol{u}^{\mathrm{k+1}}_{+}$, and negative boundary displacements $\boldsymbol{u}^{\mathrm{k+1}}_{-}$, *i.e.*

$$\boldsymbol{u}_{\mathrm{k+1}} = \begin{bmatrix} \boldsymbol{u}^{\mathrm{k+1}}_{\mathrm{int}} \\ \boldsymbol{u}^{\mathrm{k+1}}_{+} \\ \boldsymbol{u}^{\mathrm{k+1}}_{-} \end{bmatrix}, \tag{30}$$

where we have moved the $\mathrm{k}+1$ to the superscript position for the sake of legibility. According to (11), the displacements of the paired positive and negative boundary satisfy

$$u^{\mathrm{k+1},j}_{+} = u^{\mathrm{k+1},j}_{-} + \bar{\varepsilon}\,(x^{\mathrm{k+1},j}_{+} - x^{\mathrm{k+1},j}_{-}), \quad j \in \{1, 2, \ldots, p\} \tag{31}$$

where p represents the number of mapping node pairs belonging to the positive and negative boundaries. Therefore, (31) can be restated as

$$\boldsymbol{u}^{\mathrm{k+1}}_{+} = \boldsymbol{u}^{\mathrm{k+1}}_{-} + \boldsymbol{g}^{\mathrm{k+1}}, \tag{32}$$

where $\boldsymbol{g}^{\mathrm{k+1}}$ is calculated from the macroscopic strain tensor $\bar{\varepsilon}$, *i.e.* $\boldsymbol{g}^{\mathrm{k+1}} = \bar{\varepsilon}\Delta\boldsymbol{x}^{\mathrm{k+1}}$ as shown in (11).

Accordingly, (23) can be restated by dividing the stiffness matrix $\boldsymbol{K}$, external force vector $\boldsymbol{F}_{\mathrm{k+1}}$ and contact force $\boldsymbol{f}_{c,\mathrm{k+1}}$ into the form (Nguyen et al., 2012)

$$\begin{bmatrix} \boldsymbol{K}_{\mathrm{int,int}} & \boldsymbol{K}_{\mathrm{int},+} & \boldsymbol{K}_{\mathrm{int},-} \\ \boldsymbol{K}_{+,\mathrm{int}} & \boldsymbol{K}_{+,+} & \boldsymbol{K}_{+,-} \\ \boldsymbol{K}_{-,\mathrm{int}} & \boldsymbol{K}_{-,+} & \boldsymbol{K}_{-,-} \end{bmatrix} \begin{bmatrix} \boldsymbol{u}^{\mathrm{k+1}}_{\mathrm{int}} \\ \boldsymbol{u}^{\mathrm{k+1}}_{+} \\ \boldsymbol{u}^{\mathrm{k+1}}_{-} \end{bmatrix} = \begin{bmatrix} \boldsymbol{F}^{\mathrm{k+1}}_{\mathrm{int}} + \boldsymbol{f}^{c,\mathrm{k+1}}_{\mathrm{int}} \\ \boldsymbol{F}^{\mathrm{k+1}}_{+} + \boldsymbol{f}^{c,\mathrm{k+1}}_{+} \\ \boldsymbol{F}^{\mathrm{k+1}}_{-} + \boldsymbol{f}^{c,\mathrm{k+1}}_{-} \end{bmatrix}. \tag{33}$$

Substituting (32) into (33), $\boldsymbol{u}^{\mathrm{k+1}}_{+}$ terms are replaced by $\boldsymbol{u}^{\mathrm{k+1}}_{-}$ and $\boldsymbol{g}^{\mathrm{k+1}}$, yielding (Nguyen et al., 2012)

$$\begin{bmatrix} \boldsymbol{K}_{\mathrm{int,int}} & \boldsymbol{K}_{\mathrm{int},+} + \boldsymbol{K}_{\mathrm{int},-} \\ \boldsymbol{K}_{+,\mathrm{int}} + \boldsymbol{K}_{-,\mathrm{int}} & \boldsymbol{K}_{+,+} + \boldsymbol{K}_{+,-} + \boldsymbol{K}_{-,+} + \boldsymbol{K}_{-,-} \end{bmatrix} \begin{bmatrix} \boldsymbol{u}^{\mathrm{k+1}}_{\mathrm{int}} \\ \boldsymbol{u}^{\mathrm{k+1}}_{-} \end{bmatrix} \tag{34}$$

$$= \begin{bmatrix} \boldsymbol{F}_{\mathrm{int}} + \boldsymbol{f}^{c,\mathrm{k+1}}_{\mathrm{int}} - \boldsymbol{K}_{\mathrm{int},+}\boldsymbol{g}^{\mathrm{k+1}} \\ \boldsymbol{F}_{+} + \boldsymbol{f}^{c,\mathrm{k+1}}_{+} + \boldsymbol{F}_{-} + \boldsymbol{f}^{c,\mathrm{k+1}}_{-} - (\boldsymbol{K}_{+,+} + \boldsymbol{K}_{-,+})\boldsymbol{g}^{\mathrm{k+1}} \end{bmatrix}. \tag{35}$$

This formulation systematically reduces the number of unknowns, enhancing computational efficiency while preserving kinematic constraints. The resulting linear system is also solved using the Pardiso parallel sparse direct solver (LU decomposition) (Schenk and Gärtner, 2004).

3.6. Perturbation method solution

In the workflow of Fig. 2, four computational phases are executed within each loading step. First, the displacement is simulated to update geometric configurations and stresses. The resulting configuration is then treated as fixed for the subsequent homogenisation step. In practice, the periodicity vectors are evaluated using the nodal positions of the updated configuration at step k, which are treated as known quantities during the solution at step k + 1. Subsequent phases apply perturbation displacements (horizontal, vertical, and shear) to the updated geometry, assembling the configuration-dependent piecewise stiffness matrix **D** through the perturbation method. The perturbation magnitude is prescribed as $10^{-8}\Delta x$, where Δx denotes the characteristic model length, ensuring that the perturbation is sufficiently small to preserve the current contact configuration while providing an accurate numerical evaluation of the homogenised stiffness matrix. This enables automated updates of mechanical properties and stiffness matrices during deformation. Boundary conditions for perturbations are automatically detected based on initial configurations, as shown in Algorithm 3. Based on the input file, the top, bottom, right, and left boundaries, *i.e.*, B_t, B_b, B_r and B_l are respectively automatically defined. Accurate detection requires a rectangular, axis-aligned domain, with all boundary nodes positioned precisely (within a specified tolerance) on their corresponding edges. Node mapping is one-dimensional, ensuring a consistent top-to-bottom and right-to-left correspondence. Positive designations are assigned to the top and right boundaries and negative designations to the bottom and left boundaries, with mapping points automatically identified. Small horizontal displacement differences are applied to the right boundary and its corresponding mapping points in the second computational phase, while small vertical displacement differences are applied to the top boundary and its mapping points in the third computational phase. To induce shear strain, horizontal and vertical displacement perturbations are applied to the top and right boundaries in the fourth computational phase, respectively. Under the periodic boundary conditions used for stiffness matrix calculations, the total number of nodal variables and linear equations during Newton iteration is determined. Throughout the deformation process, boundary conditions, mapping points, and the equation system for different displacement perturbations remain consistent.

3.7. Model consistency

In this model, several assumptions are adopted to ensure consistency with the theoretical framework and numerical implementation described above. First, the formulation is based on geometrically linear kinematics, in which only infinitesimal strains are considered. Accordingly, each loading increment is restricted to small strains (typically below 1%) with respect to the current configuration. After every loading step, the piecewise macroscopic stiffness properties are updated to maintain the validity of the small-strain assumption, even in cases where the pore space undergoes significant compression or approaches complete closure. Consequently, the derived effective material properties are always evaluated and applied in the updated configuration under infinitesimal strain conditions. Second, within the framework of the perturbation-based homogenisation method, the macroscopic effective properties of the porous medium, including directional Young's modulus, Poisson's ratio, shear modulus, and Biot coefficients, are derived under the assumption of incremental linear elastic constitutive behaviour of the solid skeleton. Third, the treatment of solid contact assumes frictionless interaction, where nonlinearity arises exclusively from the contact constraints themselves, while the underlying material response and kinematic description remain linear.

The formulation accounts for accumulated geometrical changes through successive linearised problems defined on the updated configuration, while retaining infinitesimal kinematics and linear elasticity within each loading increment. Accordingly, the reported effective properties are incremental tangent moduli evaluated on the updated configuration, rather than moduli obtained from a finite-strain formulation.

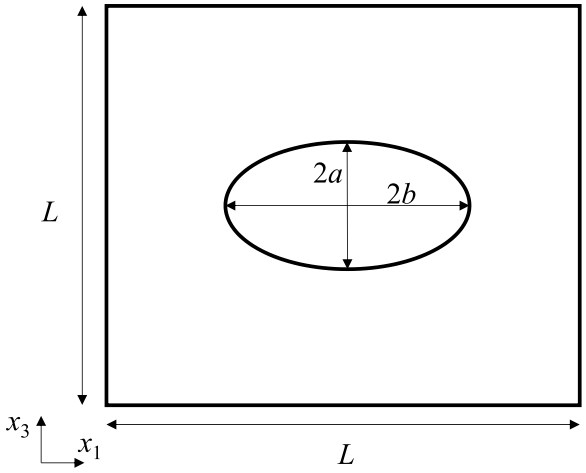


Fig. 5. The initial configuration of the model consisting of a square solid element with side length of $L = 10$ mm, including an elliptical pore with minor semi-axis a and major semi-axis b, characterised by the pore aspect ratio $R = a/b$.

4. Numerical simulations

In this section, we first conduct several simulations on simplified geometries to ensure that the contact solution and perturbation methods are validated and function as expected. We then demonstrate the numerical performance of the FA-LCP algorithm proposed in this paper. Finally, we consider several case studies of increasing complexity and demonstrate the ability of the methodology to obtain effective numerical parameters for large systems with complex contact networks. All simulations in this paper feature a solid matrix that is isotropic and linear elastic with Young's modulus $E_s = 54.2$ GPa and Poisson's ratio $\nu_s = 0.163$.

4.1. Model validation

The proposed methodology is validated stepwise, first by testing the contact detection and classification method on a problem containing two solid blocks in contact (in Appendix B.1) and the numerical homogenisation method on block of solid material (in Appendix B.2), then by comparing the results of numerical homogenisation with analytical solutions for porous media. Then, we benchmark our FA-LCP solver against two other established methods.

4.1.1. Validation of numerical homogenisation for porous media

The methodology developed in this paper is applied on a single-pore case study, allowing us to validate the results of the numerical homogenisation method against analytical solutions in the case of contactless porous geometries. The initial configuration of the single-pore model consists of a square with side length of $L = 10$ mm, containing a centrally embedded ellipse characterised by semi-minor axis a and semi-major axis b. This configuration ensures a symmetric initial model geometry where all finite elements possess positive volumes and the mesh is free from distortion or non-physical inversion, as illustrated in Fig. 5. Porosity is quantified as $n = \pi ab/L^2$, maintained constant at $n = 0.1$ across all a and b values. Under the plane strain assumption, coordinate axes are defined with the x_1-axis and x_3-axis representing horizontal and vertical directions, respectively, while the x_2-axis is perpendicular to the plane of analysis. The origin coincides with the geometric centre of the model. The pore aspect ratio R is defined as $R = a/b$. The domain is discretised into a finite element mesh comprising 1796–3501 degrees of freedom.

Algorithm 3 Automated boundary condition recognition algorithm

Require: Initial geometry configuration $\boldsymbol{x}|_{t_0}$, node coordinates
  $x_1^{\min} \leftarrow \min_i(\boldsymbol{x}_1^i|_{t_0})$, $x_1^{\max} \leftarrow \max_i(\boldsymbol{x}_1^i|_{t_0})$ ▷ Identify domain extents
  $x_3^{\min} \leftarrow \min_i(\boldsymbol{x}_3^i|_{t_0})$, $x_3^{\max} \leftarrow \max_i(\boldsymbol{x}_3^i|_{t_0})$
  $\eta_1 \leftarrow 10^{-8}(x_1^{\max} - x_1^{\min}), \eta_3 \leftarrow 10^{-8}(x_3^{\max} - x_3^{\min})$ ▷ Define boundary tolerance
  for each node i with coordinates (x_1^i, x_3^i) **do** ▷ Classify boundary nodes
    if $|x_3^i - x_3^{\max}| < \eta_3$ **then**
      $B_t \leftarrow B_t \cup$ node i ▷ Add node to top boundary set
    else if $|x_3^i - x_3^{\min}| < \eta_3$ **then**
      $B_b \leftarrow B_b \cup$ node i ▷ Add node to bottom boundary set
    end if
    if $|x_1^i - x_1^{\max}| < \eta_1$ **then**
      $B_r \leftarrow B_r \cup$ node i ▷ Add node to right boundary set
    else if $|x_1^i - x_1^{\min}| < \eta_1$ **then**
      $B_l \leftarrow B_l \cup$ node i ▷ Add node to left boundary set
    end if
  end for
  Assign positive designation to B_t and B_r
  Assign negative designation to B_b and B_l
  for each node $i \in B_t$ **do**
    $j \leftarrow \underset{j \in B_b}{\operatorname{argmin}} |x_1^i - x_1^j|$ ▷ Identify top-to-bottom mapping points
    Record mapping relationship $i \leftrightarrow j$
    $M_{tb} \leftarrow M_{tb} \cup \{(i, j)\}$
  end for
  for each node $i \in B_r$ **do**
    $j \leftarrow \underset{j \in B_l}{\operatorname{argmin}} |x_3^i - x_3^j|$ ▷ Identify right-to-left mapping points
    Record mapping relationship $i \leftrightarrow j$
    $M_{rl} \leftarrow M_{rl} \cup \{(i, j)\}$
  end for
  pass $\leftarrow$ true
  if $|B_t| = 0$ or $|B_b| = 0$ or $|B_r| = 0$ or $|B_l| = 0$ **then**
    pass $\leftarrow$ false
  end if
  if $|B_t| \neq |B_b|$ or $|B_r| \neq |B_l|$ **then**
    pass $\leftarrow$ false
  end if
  Check that all matches in M_{tb} and M_{rl} are unique
  if any node in any boundary has no mapping nodes **then**
    pass $\leftarrow$ false
  end if
  if not pass **then**
    $\eta_1 \leftarrow 10\,\eta_1$, $\eta_3 \leftarrow 10\,\eta_3$, and repeat classification
    if $\eta_1 > 10^{-3}(x_1^{\max} - x_1^{\min})$ **or** $\eta_3 > 10^{-3}(x_3^{\max} - x_3^{\min})$ **then**
      Terminate with failure: boundary recognition tolerance exceeded.
    end if
  end if
  return B_t, B_b, B_r, B_l and mapping sets M_{tb}, M_{rl}

At the initial stage, in the absence of continuous deformations, anisotropic macroscopic material properties arise due to the presence of elliptical pores. For the two-dimension plane-strain model, the incremental tangent directional Young's moduli E_1 and E_3, shear modulus G_{13} and Poisson's ratio ν_{13} are analytically determined as functions of porosity n and semi-axes a and b. In the constitutive relationship $\boldsymbol{\varepsilon} = \boldsymbol{C}\boldsymbol{\sigma}$ where $\boldsymbol{C}$ is the elastic compliance matrix (equivalent to $\boldsymbol{D}^{-1}$), we have (Tsukrov and Kachanov, 2000; Kachanov et al., 1994)

$$C_{11} = \frac{1}{E_{s1}} + \frac{\pi L_{2D}}{A\sqrt{E_{s1}}}\left[\left(a^2 - b^2\right)\cos^2\alpha + b^2 + \frac{ab}{L_{2D}\sqrt{E_{s1}}}\right], \tag{36}$$

$$C_{13} = C_{31} = -\frac{\nu_{s13}}{E_{s1}} - \frac{\pi ab}{A\sqrt{E_{s1}E_{s3}}}, \tag{37}$$

$$C_{33} = \frac{1}{E_{s3}} + \frac{\pi L_{2D}}{A\sqrt{E_{s3}}}\left[\left(b^2 - a^2\right)\cos^2\alpha + a^2 + \frac{ab}{L_{2D}\sqrt{E_{s3}}}\right], \tag{38}$$

$$C_{66} = \frac{1}{G_{s13}} + \frac{\pi L_{2D}}{A\sqrt{E_{s1}E_{s3}}}\left[\left(b^2 - a^2\right)\left(\sqrt{E_{s3}} - \sqrt{E_{s1}}\right)\cos^2\alpha + a^2E_{s3} + b^2\sqrt{E_{s1}} + abL_{2D}\sqrt{E_{s1}E_{s3}}\right], \tag{39}$$

where

$$L_{2D} = \sqrt{\frac{1}{G_{s13}} - \frac{2\nu_{s13}}{E_{s1}} + \frac{2}{\sqrt{E_{s1}E_{s3}}}}, \tag{40}$$

and E_{s1}, E_{s3}, G_{s13} and ν_{s13} denote the Young's modulus in the x_1 and x_3 directions, shear modulus and Poisson's ratio of the solid matrix without pores, respectively. α denotes the angle between the major axis of the ellipse and the horizontal direction, while A represents the representative area of the whole volume. For an isotropic solid matrix

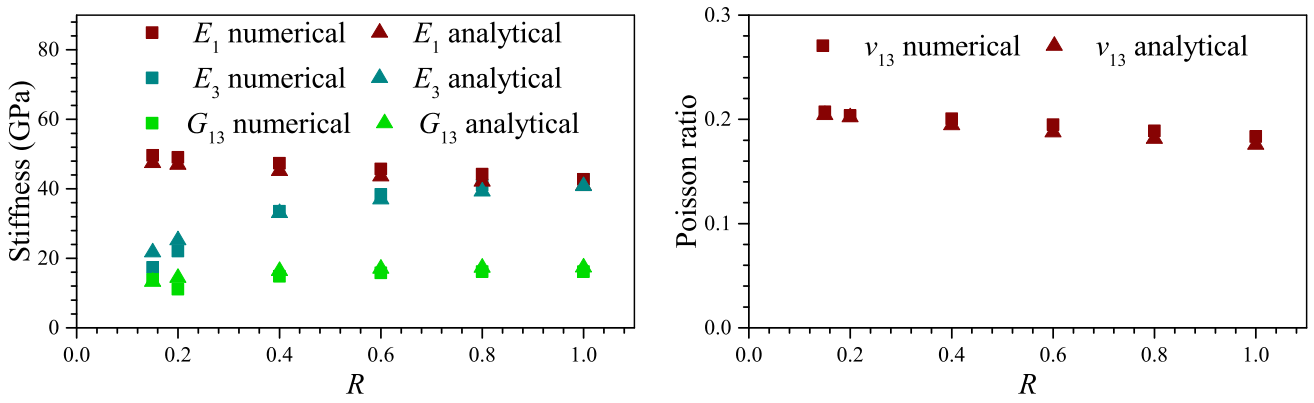


Fig. 6. Comparison of (a) Young's modulus in the x_1 and x_3 directions, shear modulus and (b) Poisson's ratio between the numerical solution and the analytical solution (Kachanov et al., 1994; Thorpe and Sen, 1985).

with zero pore orientation angle ($\alpha = 0$), we obtain

$$E_1^{2D} = \frac{E_s}{1 + n(1 + 2R)}, \tag{41}$$

$$E_3^{2D} = \frac{E_s}{1 + n\left(1 + \frac{2}{R}\right)}, \tag{42}$$

$$v_{13}^{2D} = \frac{v_{s13} E_1^{2D}}{E_s} + \frac{n E_1^{2D}}{E_s}, \tag{43}$$

$$G_{13}^{2D} = \frac{1}{\frac{1}{G_{s13}} + \frac{2n(a+b)^2}{E_s ab}}, \tag{44}$$

where the superscript 2D represents plane-strain adjustments. Specifically, these parameters are adjusted from their three-dimensional counterparts by constraining the out-of-plane strain component to zero ($\varepsilon_2 = 0$), which modifies the stress-strain relationships and leads to the apparent stiffness change typical of plane-strain formulations.

Based on (42)–(44), the mechanical parameters can be derived under 2D plane-strain conditions. However, the present model employs three-dimensional material parameters, making direct comparison between the 2D and 3D formulations inconsistent. To establish a proper correspondence, the 2D plane-strain predictions are reconciled with the 3D elasticity theory, ensuring that the effective in-plane mechanical responses under plane-strain conditions remain consistent with those obtained from the full three-dimensional constitutive relations. Accordingly, the elastic constants are modified following Kachanov et al. (1994), Thorpe and Sen (1985)

$$E_1^{2D} = \frac{E_1}{1 - v_{23} v_{32}}, \tag{45}$$

$$E_3^{2D} = \frac{E_3}{1 - v_{21} v_{12}}, \tag{46}$$

$$v_{13}^{2D} = \frac{v_{13} + v_{12} v_{23}}{1 - v_{23} v_{32}}. \tag{47}$$

Combining with (14), we obtain

$$E_3 = \frac{{E_2}^2 E_3^{2D} - E_2^{2D} E_3^{2D} E_2 {v_s}^2}{{E_2}^2 - E_1^{2D} E_3^{2D} v_s^4}, \tag{48}$$

$$E_1 = \frac{E_1^{2D}\left(E_2 - E_3 {v_s}^2\right)}{E_2}, \tag{49}$$

$$v_{13} = \frac{v_{13}^{2D}}{E_1^{2D}} E_1 - \frac{{v_s}^2}{E_2} E_1. \tag{50}$$

The analytical solution of the elastic constants is compared with the numerical results, as shown in Fig. 6. It is noted that for pore aspect ratios $R > 0.2$, the analytical and numerical solutions exhibit strong agreement, confirming the validity of the numerical framework. However, discrepancies emerge for smaller R values (especially $R = 0.15$). This deviation arises because the mesh quality deterioration and shape distortion arise with the small initial pore aperture.

4.1.2. Benchmarking of LCP solvers

As introduced above, several established and well-validated approaches have been developed for solving LCPs in solid contact problems. In this study, two classical LCP solvers are implemented for comparison, both of which directly solve (25) to obtain the optimal complementarity solution. The first approach is Lemke's method (Lemke and Howson, 1964; Lemke, 1965). This method introduces an artificial covering variable, performs an initial pivot to include the artificial variable in the basis, and subsequently pivots complementary variable pairs until the artificial variable leaves the basis or no admissible pivot can be identified. The second approach is the Projected Gauss–Seidel (PGS) solver for LCPs (Jourdan et al., 1998; Jean, 1999). The PGS method solves the complementarity conditions sequentially by updating one component at a time while holding all remaining components fixed. For the (i)-th contact degree of freedom, the unconstrained scalar update is obtained from the local equation ($\boldsymbol{u}_{\mathrm{N},k+1,i}$=0) and subsequently projected onto the admissible set

$$(\boldsymbol{f}_{c,k+1,i}) \leftarrow \max\left(0, -\frac{\left(-\boldsymbol{B}_c \boldsymbol{K}^{-1} \boldsymbol{F}_{k+1} + \boldsymbol{c}_{\mathrm{N},k}\right)_i + \sum_{j \neq i} (\boldsymbol{B}_c \boldsymbol{K}^{-1} \boldsymbol{B}_c^{\top})_{ij} (\boldsymbol{f}_{c,k+1,j})}{(\boldsymbol{B}_c \boldsymbol{K}^{-1} \boldsymbol{B}_c^{\top})_{ii}}\right). \tag{51}$$

During each sweep, newly computed values are immediately employed in subsequent updates according to the Gauss–Seidel strategy. The iterative procedure is repeated until the prescribed convergence criterion is satisfied.

Both the Lemke and PGS algorithms were implemented in Fortran 90 by directly translating the corresponding C routines provided in Siconos (Acary et al., 2019), without introducing additional numerical procedures or algorithmic modifications. The semismooth Newton algorithm, based on the Fischer–Burmeister reformulation of the complementarity conditions (Fischer, 1992, 1995, 1997), was also implemented in the same manner. Each solver is incorporated as a subroutine at the same level within the present computational framework and is supplied with the same LCP system generated by the preceding contact-detection and contact-classification procedures, and exploits the same linear algebra backend OneMKL. The semismooth Newton implementation consistently failed to converge for the contact problems considered in this study and is therefore not included in the subsequent performance comparisons.

The computational performance of the different LCP solution strategies is tested on three representative compression cases: a single-pore configuration with the same material parameters as the contactless test (Fig. 5) with $R = 0.2$, characterised by a relatively fine mesh; a single-pore configuration with $R = 0.8$, employing coarser discretisation; and a six-pore configuration representing a more complex contact topology (Fig. 7).

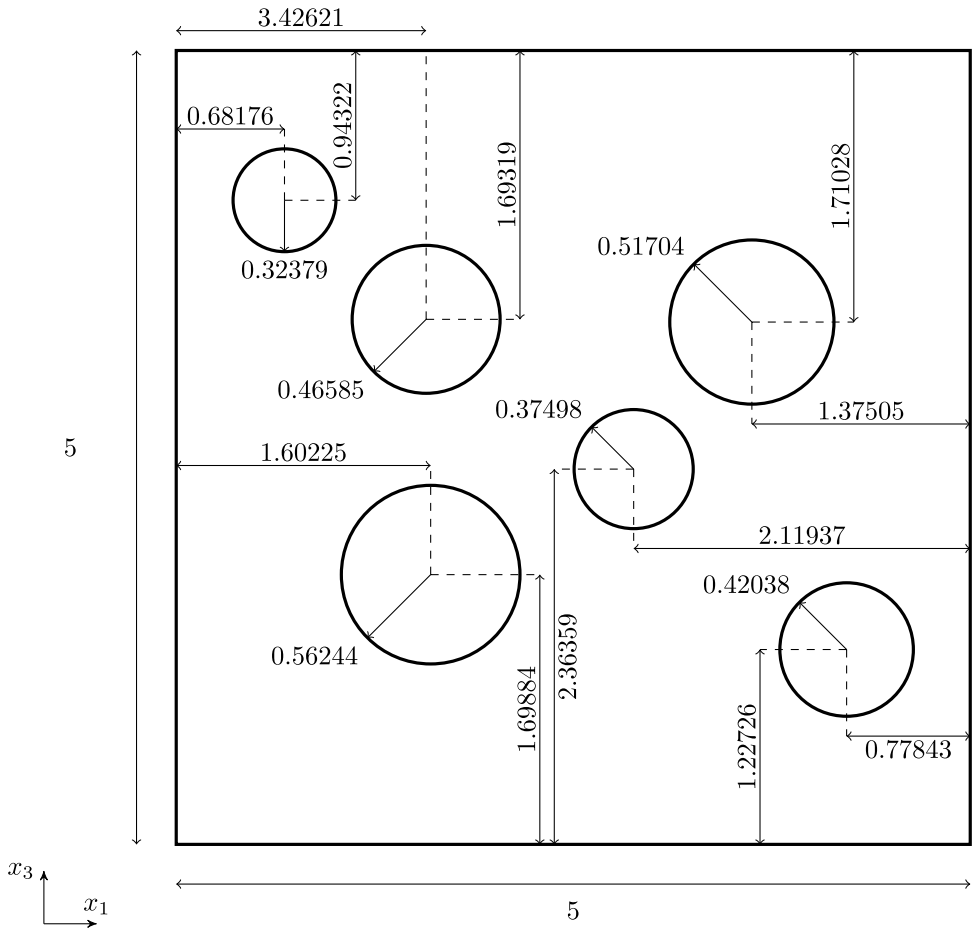


Fig. 7. The initial configuration of the model consisting of multiple pores of random sizes and spatial distributions. All dimensions are in units of millimetres.

The performance is compared in Fig. 8, including the accumulated CPU time required for LCP resolution, instantaneous memory consumption, and peak memory usage throughout the simulation. These metrics provide a comprehensive assessment of computational efficiency and resource requirements. For consistency, all simulations are performed on a workstation equipped with an Intel® Core™ i7-10750H CPU (6 cores, 12 threads, 2.60 GHz) and 16 GB RAM. Unless otherwise stated, all simulations are executed using a single computational process under identical computational environments, mesh discretisations, loading increment schemes, and convergence tolerance.

As shown in Fig. 8, before contact, all three algorithms resolve the problem quasi-instantaneously. The three algorithms detect first contact at the same total displacements (for $R = 0.8$ at 3.66 mm, for $R = 0.2$ at 1.6 mm, for 6-pore case at 2.9 mm). After contact, the CPU time and memory usage increases for all three algorithms. However, the computational costs differ markedly among the three approaches. The PGS solver exhibits the lowest computational efficiency, requiring substantially more CPU time than Lemke's algorithm. Specifically, the CPU time required by the PGS solver is approximately 3.1–16.6 times that of Lemke's algorithm, whereas Lemke's algorithm requires approximately 13.5–72.5 times the CPU time of the proposed FA-LCP method. Consequently, the proposed FA-LCP method reduces the computational cost by approximately one order of magnitude compared with Lemke's algorithm and by up to two orders of magnitude compared with the PGS solver. The efficiency advantage becomes increasingly evident as the number of active contact constraints grows during pore deformation and closure. Despite these significant differences in computational time, all methods exhibit comparable memory requirements, with only minor variations observed in both instantaneous and peak memory consumption.

The solution accuracy is further assessed using the single-pore case with $R = 0.8$ as a representative example, as shown in Fig. 9. The evolution of the active contact groups, total contact force, penetration, and Young's modulus E_1 during vertical loading is compared among the three approaches. The model contains 1698 nodes, corresponding to 3316 displacement degrees of freedom and 240 candidate contact groups. Throughout the contact stage, the displacement degrees of freedom and the candidate contact groups remain unchanged, while the active contact groups and contact forces evolve as more elements come into contact. The convergence tolerance for the contact-constrained system is set to 1×10^{-5}, and convergence is typically achieved within 2–3 iterations, ensuring that the nonlinear contact iterations do not materially affect the reported efficiency comparison.

As shown in Fig. 9, all three approaches produce consistent results for the total contact force, and effective stiffness. Although small differences are observed in the identified active contact groups, these differences have negligible influence on the resulting contact forces. Penetration is defined as the maximum overlap among all contacting surfaces. Despite minor fluctuations during contact activation, the penetration remains below 5×10^{-7} mm throughout the contact process, indicating that the contact constraints are effectively satisfied. The effective stiffness, represented by the Young's modulus E_1, also shows close agreement among the three approaches. These results demonstrate that the proposed FA-LCP method achieves substantial

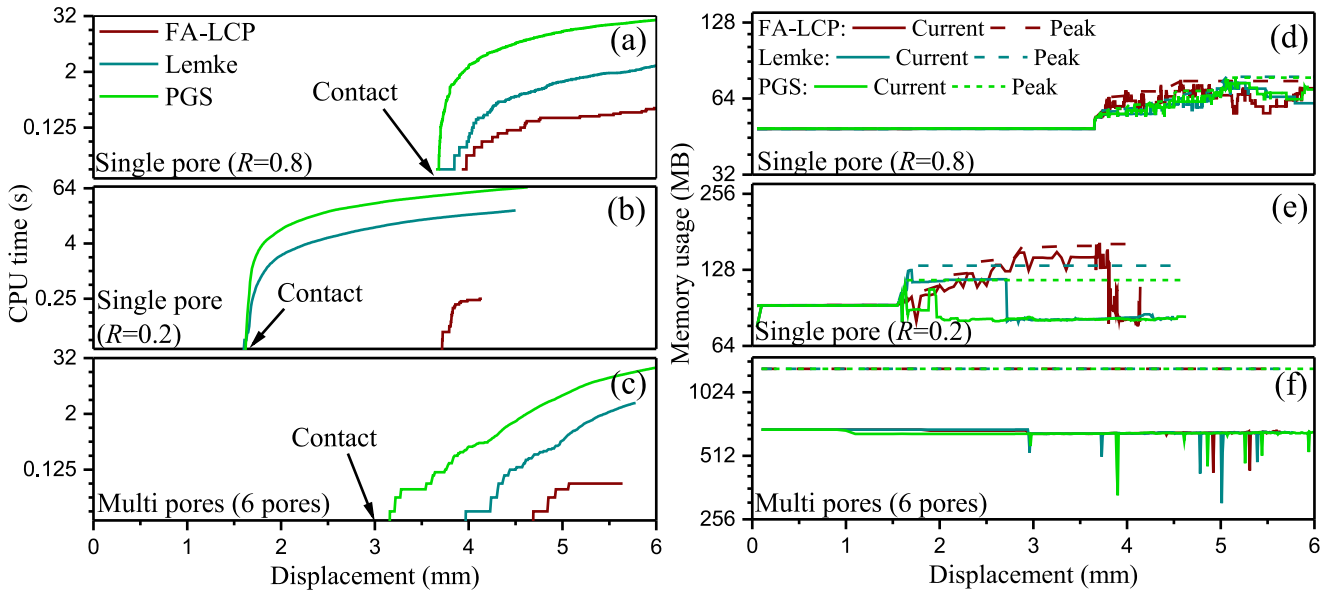


Fig. 8. Comparison of different LCP solution methods for the solid contact problem in terms of (a–c) accumulated CPU time for LCP solution (s), (d–f) instantaneous memory consumption, and peak memory usage (MB) of different cases.

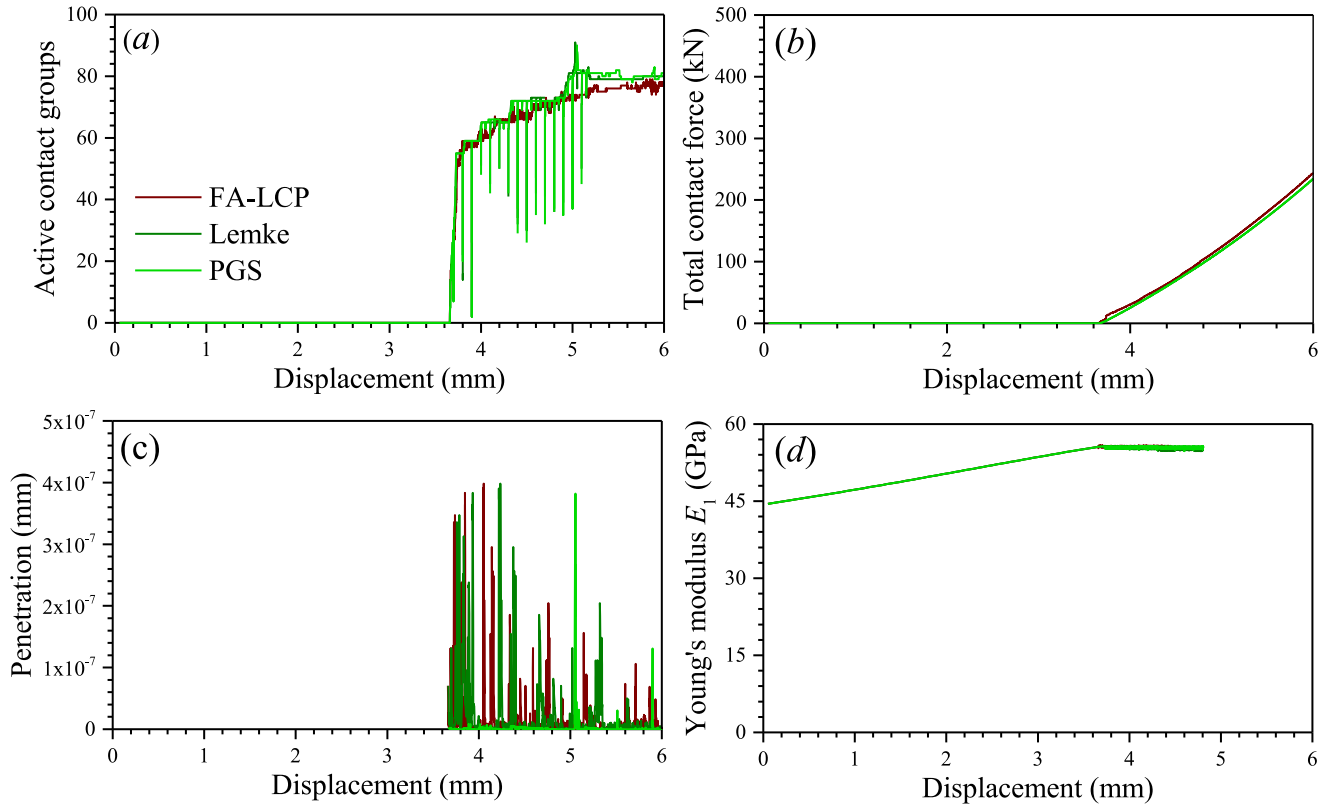


Fig. 9. Comparison of different LCP solution methods for the solid contact problem in the single-pore case with $R = 0.8$ in terms of (a) active contact groups, (b) total contact forces, (c) penetration, and (d) Young's modulus E_1 of different cases.

computational acceleration while maintaining accuracy and numerical robustness comparable to the established LCP solvers.

4.2. Mesh sensitivity analysis

A mesh sensitivity analysis is conducted for the single-pore configuration with $R = 0.8$ to assess the robustness of the numerical results with respect to spatial discretisation. Three meshes containing 1698, 3522, and 6716 nodes are considered. The corresponding effective stiffness, represented by Young's modulus E_1, the total contact force, and the mesh quality are evaluated, as summarised in Fig. 10(a)–(c). The mesh quality is characterised by the Jacobian ratio, defined as the maximum ratio of the largest to the smallest Jacobian determinant evaluated at the Gaussian integration points within each element. The calculated Young's modulus and total contact force exhibit negligible variation with increasing mesh density, indicating that the adopted

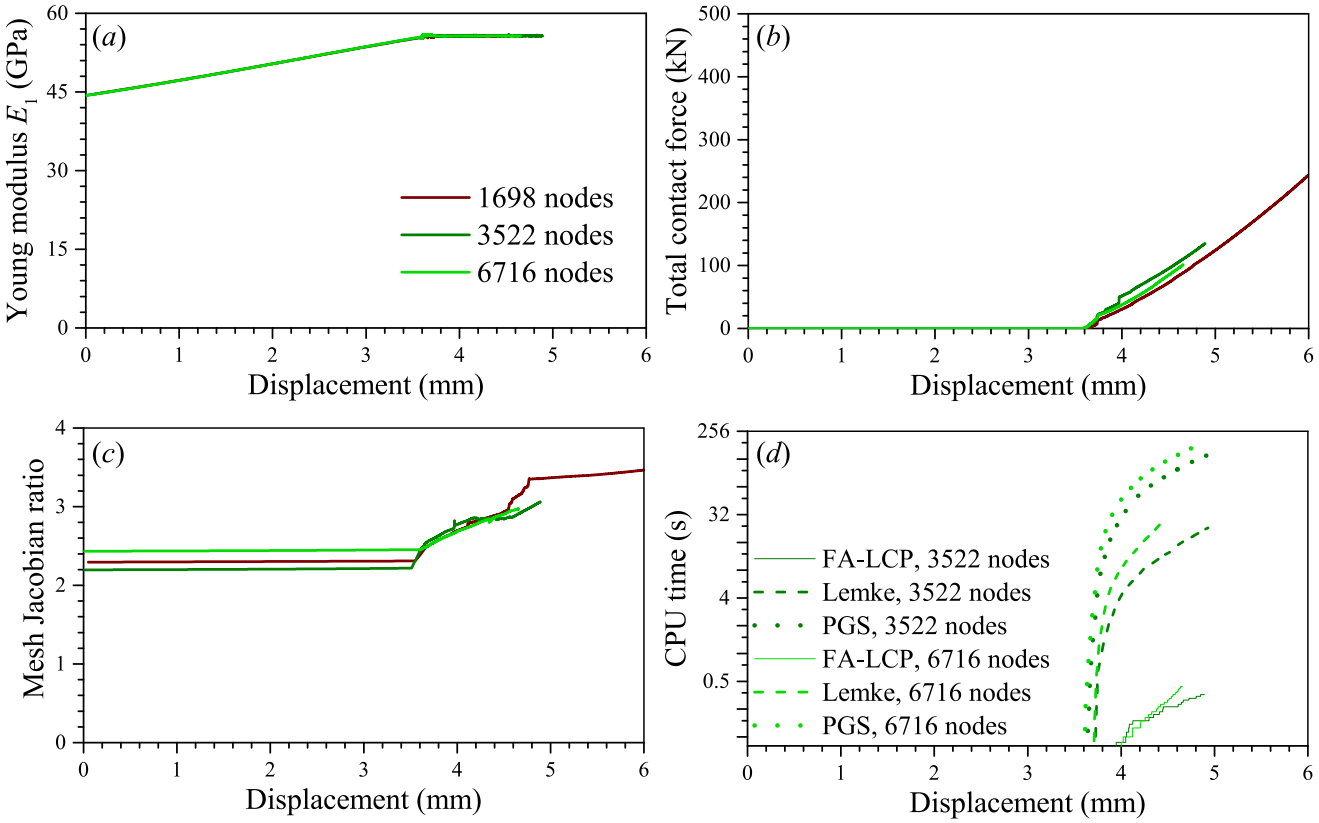


Fig. 10. Mesh sensitivity and computational efficiency of the LCP solution methods for the solid contact problem in the single-pore case with $R = 0.8$: (a) Young's modulus E_1, (b) total contact force, (c) Jacobian ratio, and (d) CPU time for increasing mesh resolution.

discretisation provides mesh-converged predictions of both the global stiffness response and contact interaction. Although the coarsest mesh yields a slightly larger Jacobian ratio, with a maximum value of approximately 3.5, this value remains sufficiently low to avoid significant element distortion. Further mesh refinement therefore produces only marginal changes in the mechanical response while increasing the computational cost. Hence, the system with 1698 nodes is adopted for all further analysis.

The computational cost of the LCP calculation is further compared for the three solution strategies in Fig. 10(d). The proposed FA-LCP framework consistently exhibits a substantial computational advantage over the conventional Lemke and PGS algorithms, and this advantage becomes even more pronounced for the finer discretisation. For the mesh with 3522 nodes, the CPU times required by the Lemke and PGS solvers are approximately 46 and 324 times that of the proposed FA-LCP method, respectively. With 6716 nodes, these ratios increase to approximately 86 and 399, respectively. These results demonstrate that the relative computational efficiency of the proposed FA-LCP framework increases as the problem size increases.

4.3. Model application to porous materials

Application of the proposed methodology on porous media is demonstrated through different examples of 2D pore geometries. First, we show how homogenised properties evolve in a simple element with a single pore under multidirectional loading. Then, we show the same application on an element with six pores. Finally, a simulation of a more complex porous material, containing 180 pores, is analysed.

4.3.1. Application to single-pore case

Our framework is now applied to a simple single pore case to analyse multidirectional deformations in the model with an initial pore aspect ratio $R = 0.8$, focusing on the evolving piecewise stiffness matrix and mechanical properties in updated configurations. Three distinct loading scenarios are implemented so the geometric but not constitutive nonlinearity is modelled. To satisfy the small-strain assumption, the mechanical properties are updated incrementally after each loading step while maintaining the local strain below approximately 1%. First, horizontal compression is imposed by prescribing a displacement increment on the lateral boundaries. The displacement rate is defined as $u_1 = -1 \times 10^{-2}$ mm per step prior to solid contact and $u_1 = -1 \times 10^{-3}$ mm per step after contact initiation. The right boundary is assigned a negative horizontal displacement, corresponding to compression of the representative volume element (RVE), while vertical displacements on the boundaries are constrained to zero. Under this loading condition, the pore progressively closes until solid contact develops between opposite pore surfaces, accompanied by the evolution of internal contact stresses. Second, vertical compression is applied through prescribed displacement increments on the top and bottom boundaries. The vertical displacement rate is specified as $u_3 = -1 \times 10^{-2}$ mm per step before solid contact and $u_3 = -1 \times 10^{-3}$ mm per step after contact initiation. The top boundary is subjected to negative vertical displacement, while horizontal displacements are constrained, thereby inducing macroscopic vertical strain within the RVE. Third, shear deformation is generated by simultaneously applying tangential displacement increments on all boundaries. Vertical displacements are prescribed on the left and right boundaries with rates of $u_{13} = 1 \times 10^{-2}$ mm per step before solid contact and $u_{13} = 1 \times 10^{-3}$ mm per

step after contact initiation. Concurrently, horizontal displacements are imposed on the top and bottom boundaries with rates of $u_{31} = 1 \times 10^{-2}$ mm per step before contact and $u_{31} = 1 \times 10^{-3}$ mm per step after contact. This loading configuration produces macroscopic shear displacement and shear strain within the porous structure.

After compressing and shearing the model over loading in different directions, the pore in the solid matrix is compressed, resulting in a decrease in total porosity, as shown in Fig. 11(a). The deformation behaviour exhibits pronounced nonlinearity, primarily due to geometric effects as the pore shape changes. For the initial $R = 0.8$, the porosity reduction under shear displacement initially lags behind that induced by horizontal and vertical displacements, but then accelerates rapidly, reaching effectively zero at a cumulative displacement of $u_{13} = 3.1$ mm. Porosity reduction under horizontal compression proceeds more slowly than under vertical compression, with pore closure occurring at $u_1 = 4.6$ mm versus $u_3 = 3.6$ mm for the vertical loading. After complete pore closure, the porosity remains close to zero, confirming the consistency of the compaction behaviour.

During the compression process, the stress distribution evolves significantly, which can be divided into contactless and contact stages, as shown in Fig. 11(b–c). Due to the initial pore aspect ratio $R = 0.8$, vertical compression reduces the pore aspect ratio, resulting in a more elongated pore shape, while horizontal compression initially increases the aspect ratio, first leading to a more uniform pore shape and later an elongated pore along the vertical direction with $R > 1.0$. Stress concentrations develop at the pore tips and the contacting surfaces, particularly in circumferential directions, intensifying with increasing strain. Tensile stress concentration dominates near pore midlines in the circumferential direction, whereas compressive stress concentration prevails at pore tips in the circumferential direction. Shear stress changes remain small compared to horizontal and vertical stresses. Post-contact, normal contact tractions on the internal interfaces prevent the overlap of internal boundaries; however, their magnitudes remain minimal and negligible relative to stresses within the solid matrix.

The evolving model configuration necessitates on-the-fly updates to the piecewise stiffness matrix and mechanical properties in accordance with (36)–(39). Fig. 12 illustrates the evolution of incremental tangent Young's modulus (E_1 and E_3), shear modulus (G_{13}), Poisson's ratio (ν_{13}), and Biot coefficients (b_1, b_2, and b_3) during multidirectional loading. Under uniaxial compression, Young's modulus decreases in the loading direction while increasing linearly in the orthogonal direction. For instance, as the applied horizontal displacement u_1 increases to 4.64 mm, E_1 decreases linearly from 44.22 GPa to 40.95 GPa, while E_3 increases linearly from 48.8 GPa to 55.58 GPa, approximately reaching E_s (54.2 GPa). When the applied vertical displacement u_3 increases to 3.6 mm, E_3 decreases linearly from 41.04 GPa to 37.58 GPa, while E_1 increases linearly from 44.28 GPa to 55.68 GPa (approximately E_s). This directional trend results from the geometric distortion of the elliptical pore. Compression reduces the effective load-bearing area along the loading direction while simultaneously elongating the pore laterally, which stiffens the material in the orthogonal direction. This trend is consistent with the analytical expression in (41)–(42), in which the incremental tangent Young's modulus depend on the pore aspect ratio R. As R increases, the modulus along the minor-axis direction increases, whereas the modulus along the major-axis direction decreases. Following solid contact, the incremental tangent Young's moduli in different directions under horizontal or vertical compression progressively approach the solid stiffness E_s, particularly in the loading direction, where a pronounced jump increase is observed. In contrast, shear loading leads to a reduction in the incremental tangent Young's modulus in all directions before solid contact. Under combined shear loading (simultaneous applied displacements of 3.1 mm on the right and left boundaries and applied horizontal displacements of 3.1 mm on the top and bottom boundaries), both E_1 and E_3 decrease, from 44.22 GPa to 37.6 GPa and 41.05 GPa to 33.73 GPa, respectively. Post-contact, a further increase in displacement to 3.4 mm reverses this trend, driving E_1 and E_3 up to 47.58 GPa and 47.11 GPa. Nevertheless, both moduli remain lower than the stiffness of the intact solid, E_s.

As compression or shear displacement in different directions increases over loading, the incremental tangent shear modulus G_{13} increases, while incremental tangent Poisson's ratio ν_{13} decreases before solid contact. Horizontal compression exerts the most significant influence, increasing G_{13} by 3.13 GPa until solid contact, compared to 2.30 GPa under vertical compression and 0.22 GPa under shear displacement, with the growth rate accelerating over loading. However, after solid contact and without considering friction, G_{13} exhibits an abrupt increase under different loading modes, approaching the solid shear modulus G_s during the compression process but reaching about 20.8 GPa during shearing process which remains slightly lower than G_s.

The incremental tangent Poisson's ratio ν_{13} exhibits inverse proportionality to displacement magnitude, with the incremental tangent shear displacement causing the most pronounced reduction rate and vertical compression the least, as shown in Fig. 12(d). During pre-contact deformation, ν_{13} decreases by 0.026, 0.068, and 0.045 until solid contact under horizontal, vertical, and shear displacements, respectively. Following contact initiation, the evolution of ν_{13} diverges depending on the loading mode. Under horizontal compression, ν_{13} exhibits an abrupt increase and rapidly approaches the value under vertical loading, which is close to the solid Poisson's ratio ν_s. In contrast, under shear loading, ν_{13} overshoots ν_s immediately after solid contact and subsequently decreases as the contacting pore surfaces undergo rotational rearrangement and sliding while maintaining contact.

Biot coefficients demonstrate directionally dependent behaviour, as presented in Fig. 12(e). The transverse coefficient b_2 (in the x_2-direction) decreases monotonically across all loading modes. In contrast, the axial coefficients b_1 (in the x_1-direction) and b_3 (in the x_3-direction) exhibit opposite responses. Uniaxial compression increases the Biot coefficient in the loading direction while reducing it in the orthogonal direction, whereas shear loading elevates both b_1 and b_3. Following solid contact, the Biot coefficients exhibit a pronounced abrupt decrease, particularly under horizontal and vertical compression, where they progressively approach zero. These directional variations are inversely correlated with the evolution of Young's modulus, thereby underscoring the significance of elastic coupling effects on the evolution of incremental (tangent) effective poroelastic properties. In addition, progressive shear displacement induces a transition from a symmetric anisotropic configuration to an asymmetric state, as shown in Fig. 11(b), manifesting as non-zero shear-coupling stiffness coefficients D_{16}, D_{26}, and D_{36} in (12). These parameters, which characterise normal–shear strain coupling effects that are important to accurately capture the constitutive behaviour of geomaterials, remain zero during purely horizontal or vertical compression where model symmetry is preserved. Fig. 12(f) shows the evolution of these parameters, D_{16}, D_{26}, and D_{36}, during shear displacement. They exhibit near-linear increases from 0 to 6.85 GPa, 2.19 GPa, and 6.60 GPa, respectively, at a shear displacement of 3.1 mm. Following internal boundary contact, D_{16}, D_{26}, and D_{36} exhibit sharp decrease to less than 0.5 GPa. This shear-induced coupling, typically neglected in conventional stiffness formulations, underscores the necessity of constitutive models with nonlinear elasticity at the RVE scale for anisotropic media undergoing multidirectional loading.

However, as observed, slight oscillations appear in the evolution of the piecewise stiffness parameters after solid contact is established. This behaviour is mainly related to the numerical treatment of the contact constraints rather than to any physical instability. In situations involving nearly simultaneous multi-contact or transitions between active constraint sets, small perturbations in the active set identification or numerical tolerances may lead to slight variations in the computed

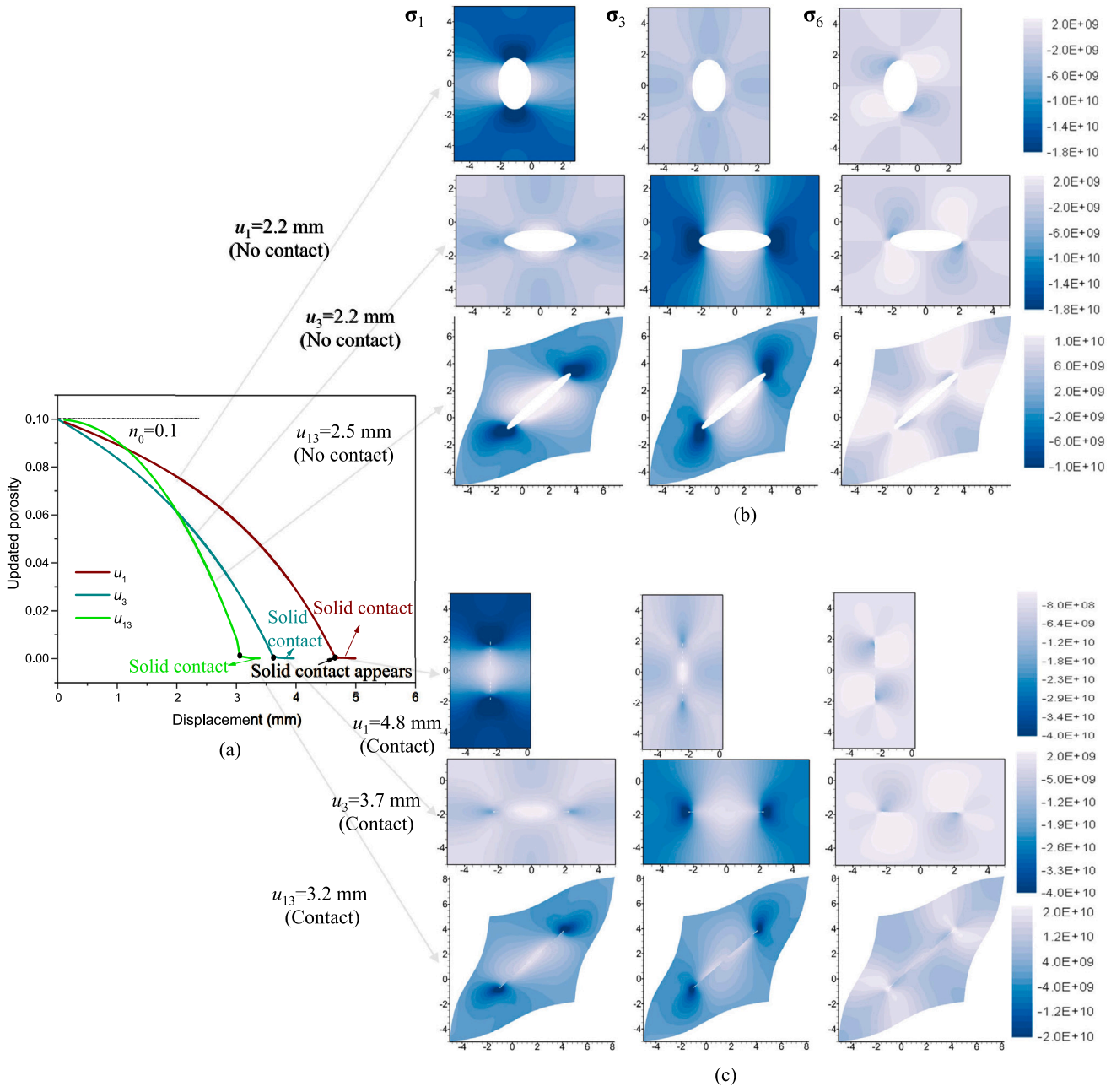


Fig. 11. Evolution of (a) porosity, (b) horizontal normal stress σ_1, vertical normal stress σ_3, and shear stress σ_6, before contact, and (c) stress states after contact during progressive multidirectional compression loading.

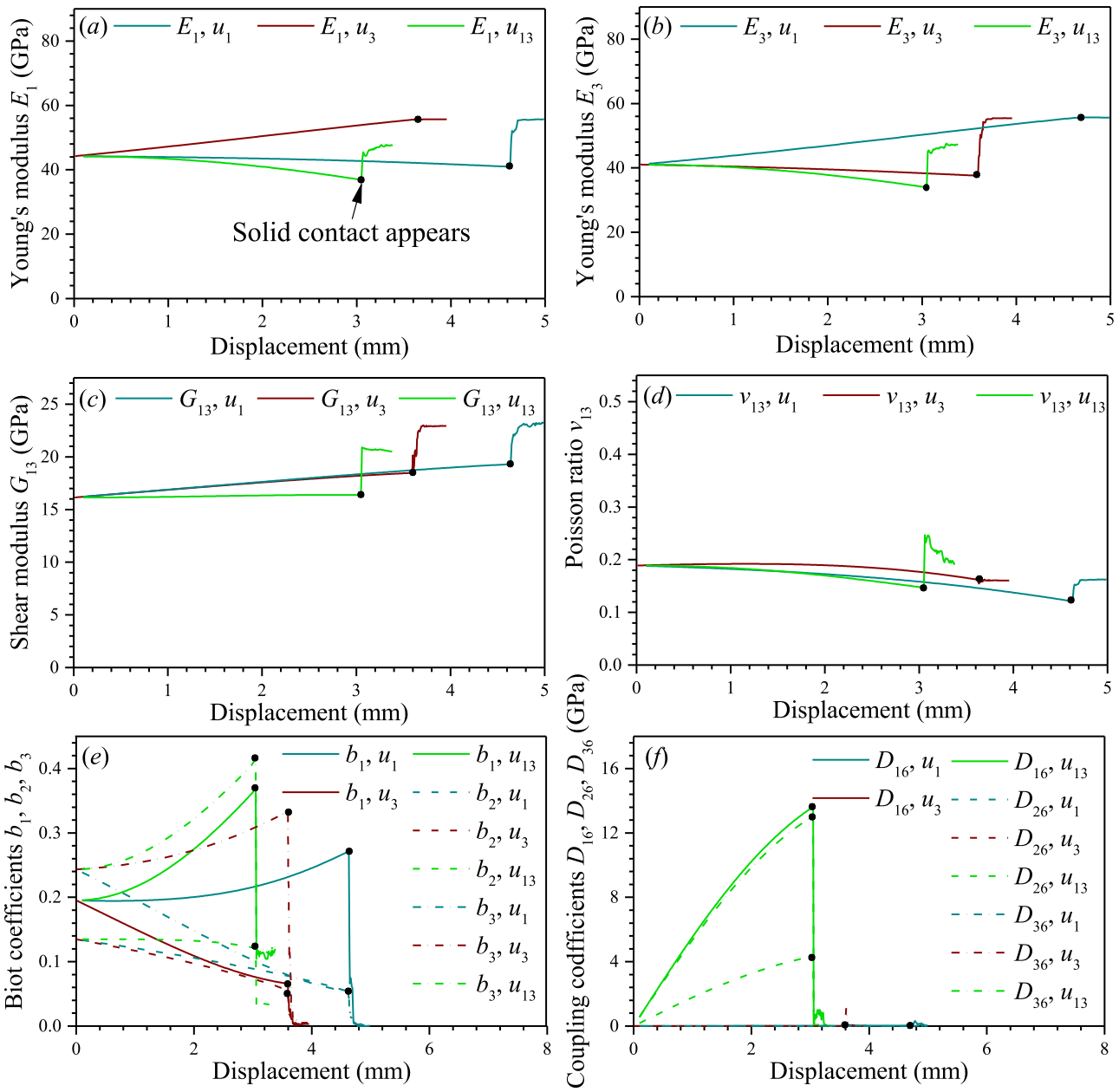


Fig. 12. Evolution of the effective system parameters under vertical, horizontal and shear deformations. (a) incremental tangent Young's modulus E_1, (b) incremental tangent Young's modulus E_3, (c) incremental tangent shear modulus G_{13}, (d) incremental tangent Poisson's ratio ν_{13}, (e) incremental tangent Biot coefficient in different direction b_1, b_2 and b_3, and (f) Shear coupling moduli D_{16}, D_{26} and D_{36}.

displacements, which in turn induce minor oscillations in the tangent stiffness parameters. We emphasise that these oscillations are purely numerical artefacts. In our simulations, the deviations remained below the prescribed tolerance (generally less than 1×10^{-5}) within the numerical calculation workflow shown in Fig. 2. Moreover, these small discrepancies did not propagate to the macroscopic level and had a negligible influence on the homogenised stress response.

To further assess the significance of these variations, the relative local stiffness oscillations are further quantified as the absolute second-order difference of the tangent stiffness normalised by the average stiffness over three consecutive loading steps. For Young's modulus, Poisson's ratio, and shear modulus in different directions under different loading conditions, the average oscillation is approximately 0.06%, with a maximum of 3.8%. For the Biot coefficients under shear loading, the corresponding average and maximum oscillations are approximately 0.85% and 5.91%, respectively. The oscillations remain small relative to the overall evolution of the homogenised parameters and do not produce a discernible change in the homogenised stress–strain response. The relatively larger maximum oscillations occur only locally and do not represent a systematic deviation in the overall stiffness evolution. These local oscillations can be reduced by incrementally averaging the homogenised tangent stiffness over consecutive loading steps.

4.3.2. Application to six-pore case

The developed model and simulator are further applied to a two-dimensional square domain with side length $L = 5$ mm, in which multiple pores of random sizes and spatial distributions are embedded, as shown in Fig. 7. The initial porosity is defined as the area fraction $n = \sum(\pi r_i^2)/L^2$, where r_i denotes the radius of the ith pore. The displacement loading scheme and periodic boundary conditions are implemented in the same manner as in the single-pore case and

Table 1
Corresponding displacement (mm) associated with progressive pore contact and complete closure under different loading modes.

Loading mode	1st contact	2nd contact	3rd contact	4th contact
Vertical	2.9	3.67	3.7	4.19
Horizontal	3.2	4.0	4.1	4.4
Shearing	3.0	3.11	3.27	3.82
Loading mode	5th contact	6th contact	Fully closed	
Vertical	4.21	4.32	5.07	
Horizontal	4.5	4.8	5.07	
Shearing	4.68	4.9	5.23	

then the piecewise stiffness properties are updated. This configuration enables the simulation of pore–matrix interactions during progressive loading and provides a framework for examining how staged pore contact influences the evolution of the global stiffness matrix and Biot coefficients. By subjecting the model to vertical, horizontal, and shear displacements, the study captures not only the porosity-driven stiffening process but also the anisotropic effects arising from sequential pore contact and closure.

Figs. 13 and 14 show the evolution process of different mechanical properties and pore contact behaviour under vertical, horizontal, and shear compression. The results reveal a strongly nonlinear and path-dependent poromechanical evolution under these loading conditions. As external displacement increases, pores undergo a staged transition from gradual flattening to localised pore wall contact and ultimately to full closure, as summarised in Table 1.

The transition between the different loading stages is governed by pore size and pore position, with smaller pores closing earlier and larger pores closing later. For normal loading, pores closer to the loading axis (along the normal direction of the applied load boundary) consistently initiate contact earlier, whereas for shear loading, pores closer to the compressed angles initiate contact earlier while the middle pores close later. The effective porosity evolution therefore follows a nonlinear trajectory, with an initial acceleration due to pore flattening, followed by a deceleration as multiple pore contacts emerge, and finally a slow approach to zero porosity once the contact network saturates.

The staged contact mechanism influences the evolution of piecewise stiffness and poromechanical coefficients, with responses differing markedly between normal (vertical and horizontal) compression and shear loading. These trends are broadly consistent with those identified in the above single-pore case, though additional effects emerge from the collective interactions among multiple pores. Specifically, before solid contact, the effective Young's modulus in the loading direction decreases continuously with displacement, whereas the modulus in the orthogonal direction increases as pores are progressively flattened. This behaviour is due to the geometric evolution of pores and the corresponding load transfer modes. For example, under vertical compression, the vertical dimension of pores shrinks, reducing the solid thickness around pores available to sustain axial loads. As these load-bearing paths become thinner, deformation is increasingly bending-dominated, leading to a rapid decline in vertical stiffness. Conversely, in the orthogonal direction, pore flattening increases the continuous solid fraction, enhancing stretching resistance and thereby raising the modulus. Once contacts occur, the increase in orthogonal stiffness becomes significantly attenuated, as the strengthening mechanism reaches a saturation point close to E_s. In contrast, the loading-direction stiffness increases and eventually converges to a value comparable to that in the orthogonal direction. Specifically, each successive staged contact of different pores induces a discrete jump in stiffness along the loading direction. In addition, shear displacement before solid contact leads to a continuous decrease in the Young's modulus in different directions. This behaviour mirrors the single-pore case, but the effect is amplified in multi-pore systems. Under shear, pores deform asymmetrically and undergo relative sliding, which disrupts load-bearing continuity across the matrix. Once solid contact is formed, however, stress can be directly transmitted across contacting regions, resulting in a pronounced increase in stiffness in all directions. However, because contact friction is neglected in the present model, the stiffness cannot fully recover to that of the intact solid, even under conditions of complete pore contact.

The evolution of the incremental tangent shear modulus (G_{13}) and Poisson's ratio (ν_{13}) under multidirectional loading exhibits a distinct behaviour compared to the effective Young's moduli. In any compression mode, G_{13} initially increases slowly as pores are progressively flattened, since oblique load-transfer paths within the solid skeleton become more effective in sustaining shear resistance. Further, after staged pore contact, G_{13} increases markedly and continues until full contact is achieved. This enhancement arises because contacting pore walls tend to rotate relative to one another under shear loading; such rotational interactions intensify stress transmission across the contact interfaces, thereby strengthening the shear response. The response of the incremental tangent Poisson's ratio (ν_{13}) further highlights the anisotropic coupling. Under horizontal or vertical compression, ν_{13} decreases, especially in the later loading, reflecting constrained orthogonal contraction and diminished transverse–longitudinal coupling due to pore geometry. Once pore contacts are established, this trend reverses, and ν_{13} progressively approaches the solid Poisson's ratio ν_s as full contact is reached. The stiffening effect associated with solid contact is more pronounced under horizontal compression than under vertical compression. In contrast, under shear compression, ν_{13} increases rapidly upon contact formation but subsequently exhibits a slight decrease as rotational interactions and surface sliding between contacting pore walls develop. Overall, these observations indicate a fundamental reorganisation of load-transfer mechanisms, shifting from a skeleton-controlled regime to one dominated by the pore-contact network, consistent with the trends identified in the single-pore system.

In addition, the Biot coefficients exhibit analogous directional dependence. Under vertical or horizontal compression, pore flattening increases the effective solid fraction in the loading direction while reducing it in the orthogonal direction. Consequently, the Biot coefficient increases along the loading axis, indicating stronger coupling between pore pressure and normal stress, while it decreases transversely. As successive contacts are activated, the inferred Biot coefficients decrease markedly and approach zero after complete closure under normal compression, indicating a reduction in the inferred coupling between pore pressure and macroscopic stress. In shear loading, however, the Biot coefficients in both vertical and horizontal directions increase. This is because diagonal pore compression enhances the effective load-bearing area, thereby strengthening the coupling between fluid pressure and stress in multiple orientations. Nevertheless, the Biot coefficients still exhibit abrupt decreases during staged pore contact and remain a non-zero residual value after full contact.

In summary, the findings highlight pore contact as the dominant mechanism governing the nonlinear and anisotropic poromechanical response of porous solids. The sequential nature of pore closure not only controls the rate of stiffness evolution but also determines its directional dependence. This behaviour reflects a fundamental transition in deformation mechanisms from a regime dominated by distributed solid-skeleton deformation to one governed by localised contact networks, accompanied by stress redistribution and progressive development of an anisotropic microstructural fabric.

4.3.3. Application to complex multi-pore case

To demonstrate the applicability of the proposed FA-LCP algorithm to complex porous media, a two-dimensional square domain with side length $L = 10$ mm is considered, in which 180 pores are randomly distributed, as shown in Fig. 15. The initial porosity is 0.35. The corresponding mesh file is available as Supplementary Material. Periodic boundary conditions are imposed in the same manner. To mimic progressive compaction induced by increasing external compressive

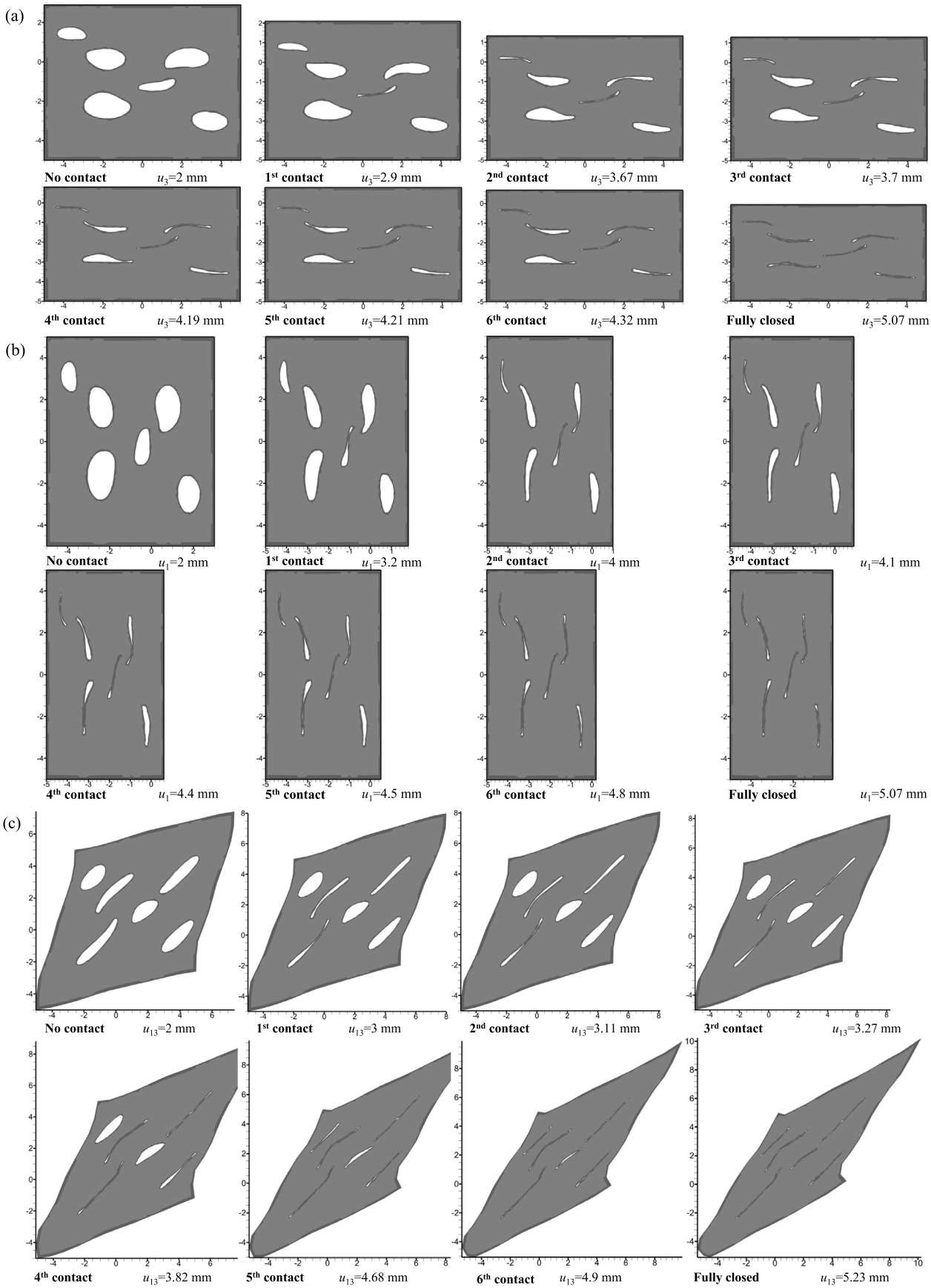


Fig. 13. Pore contact behaviour during progressive (a) vertical displacement, (b) horizontal displacement, and (c) shear displacement.

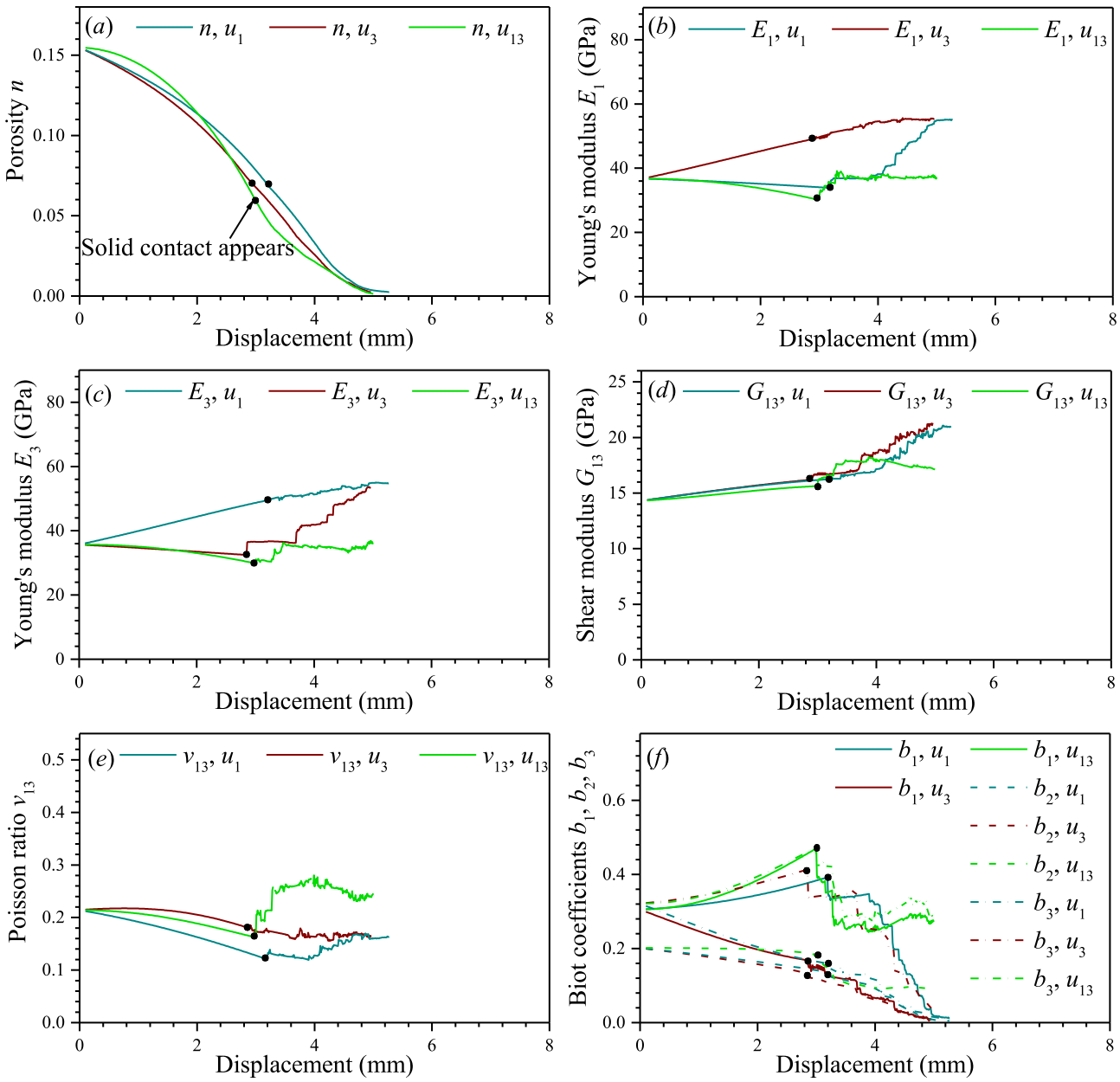


Fig. 14. Evolution of (a) effective porosity,(b) incremental tangent Young's modulus E_1, (c) incremental tangent Young's modulus E_3, (d) incremental tangent shear modulus G_{13}, (e) incremental tangent Poisson's ratio v_{13}, and (f) incremental tangent Biot coefficient in different direction b_1, b_2 and b_3, during progressive vertical, horizontal and shear displacements.

loading, only vertical compression is applied through prescribed displacement increments. As such, the problem can be taken to represent the consolidation of a highly-anisotropic porous material under increasing overburden pressure. The displacement increment is set to $u_3 = -1 \times 10^{-2}$ mm per load step before contact initiation and reduced to $u_3 = -5 \times 10^{-3}$ mm thereafter to resolve the rapid evolution of contact during pore closure. The loading scheme is consistent with the small-strain assumption adopted throughout this study.

Based on this complex multi-pore configuration, the evolution of porosity, directional incremental tangent Young's moduli, Poisson's ratio, shear modulus, and directional Biot coefficients is evaluated throughout progressive compression loading, as shown in Fig. 16. The overall trends are consistent with those observed in the simplified six-pore model. In particular, the evolution of effective properties is governed by a piecewise response associated with the onset and progression of solid contact, which may either amplify or counterbalance the effects of continued compression. With increasing compression, local pore closure and early contact formation occur in a subset of pores, while the global porosity exhibits only gradual variation. This highlights that significant changes in effective mechanical properties can arise from the development of local contact networks even when the overall porosity remains nearly unchanged. These results further demonstrate the necessity of explicitly accounting for solid contact in realistic porous media, where macroscopic property evolution is strongly governed by pore-scale contact interactions.

5. Discussion

Despite the developments and results presented above, several limitations remain in the present model and numerical methodology. First, the current implementation is restricted to a two-dimensional

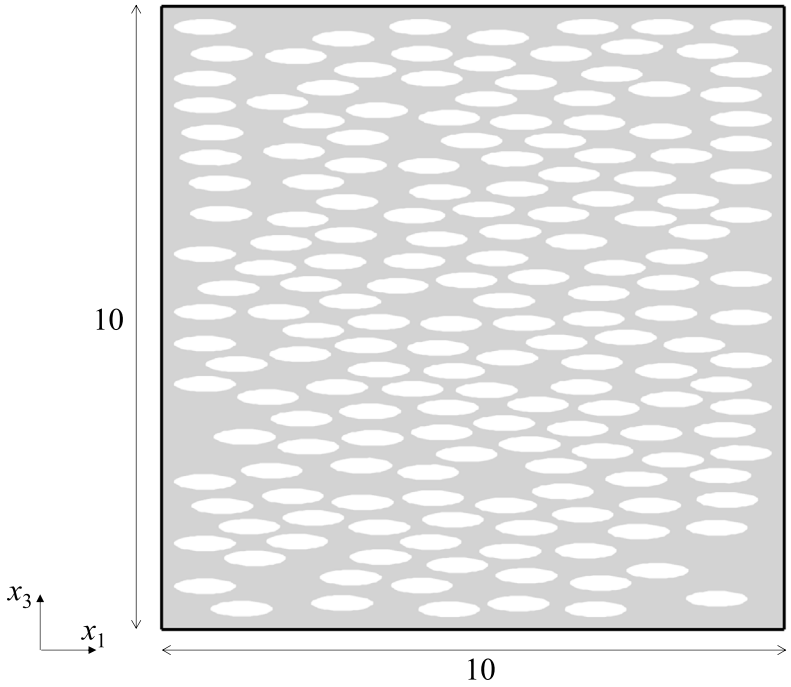


Fig. 15. Geometry of the complex multi-pore system with 180 randomly distributed pores.

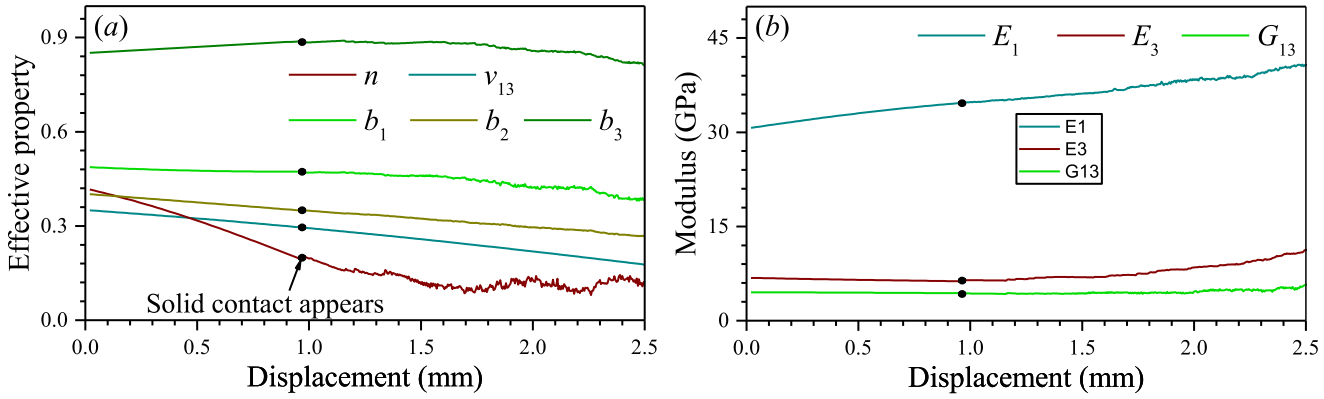


Fig. 16. Evolution of (a) effective porosity n, incremental tangent Poisson's ratio v_{13}, incremental tangent Biot coefficient in different direction b_1, b_2 and b_3, (b) incremental tangent Young's modulus E_1 and E_3 and incremental tangent shear modulus G_{13} during progressive vertical displacement.

plane strain setting. In particular, although solid contact can be robustly handled in two dimensions, the extension to face-to-face contact in 3D configurations introduces significant algorithmic and geometrical challenges. These include more complicated contact detection, constraint enforcement, and active-set identification, which have not yet been developed in the present work. Second, frictional effects within the contact group are neglected, and only frictionless normal contact is considered. While this assumption simplifies the complementarity structure and improves computational efficiency, it likely underestimates shear resistance and energy dissipation in granular or rough-contact systems. If friction were to be included, we would expect the apparent values of E_1, E_3 and G_{13} to be greater (at least initially) post-contact, as local resistance to sliding due to friction is prevented, which appears (after homogenisation) as greater elastic resistance to the applied load. However, the system may also experience increased oscillations of the apparent properties, as "frictional paroxysms" occur as individual elements transition between sticking and sliding, and so the apparent elastic resistance changes. The apparent Poisson's ratio v_{13} may increase, decrease or not change, depending on the changes in the apparent elastic stiffnesses, and no conclusion as to its likely behaviour can be drawn *a priori*. Third, the solid matrix is modelled as linear elastic, while it does not account for finite deformation or material nonlinearities such as plasticity, damage, or viscoelastic effects. Consequently, the incremental stiffness matrix is evaluated within locally updated configurations. In addition, the pore fluid pressure along the pore boundaries is assumed to be constant. Moreover, the computational domain is restricted to an axis-aligned rectangular RVE. This requirement facilitates the implementation of periodic boundary conditions and simplifies matrix assembly, but it reduces geometric flexibility.

From a numerical perspective, the objective of the solid contact treatment is to solve (10), which involves two challenges. First, the system contains two coupled unknown fields (*i.e.* the displacements and the contact forces), requiring a complex numerical solution process. Second, determining the active contact set requires checking all possible contact groups, which becomes computationally expensive for large-scale problems due to the combinatorial growth of candidate contact configurations. A major contribution of this work is the significant speedup achieved by the proposed fast approximation LCP method. However, for cases involving complex and densely distributed contact groups, slight oscillations in the post-contact stiffness parameters may occur. These oscillations are mainly induced by the approximate treatment of the active set in highly constrained configurations. These variations remain small relative to the overall stiffness evolution and do not significantly affect the homogenised mechanical response. Nevertheless, for applications that may require highly accurate local tangent responses, such as direct FEM^2 coupling, such oscillations may introduce numerical noise. In this case, incremental averaging of the homogenised tangent stiffness between consecutive loading steps can be adopted during the upscaling process. This treatment does not alter the underlying contact formulation and can be directly incorporated into the FEM^2 coupling procedure.

The framework presented in this paper can be expanded in a number of different directions in the future. Most obviously, an extension to three dimensional finite element simulations is eminently achievable, without any substantial changes needing to be made. A small caveat to the system's applicability to geomaterials is that it requires the solid material to be fully connected (and thus incapable of rigid body motions after the Dirichlet boundary conditions have been applied). However, in realistic geometries of rocks and soils it is possible to have disconnected grains that are individually capable of rigid body motions, which ultimately leads to the LU decomposition not being obtainable and the method failing. The remedy in this case is straightforward, by simply changing from quasi-statics to dynamics and specifying an impact law (typically Newton's impact law), a classical nonsmooth contact dynamics method is obtained (Dubois et al., 2018), which is easily adapted to our framework.

We note that presuming a fully-connected three-dimensional quasi-static system, a naive analysis of the scaling behaviour suggests that the speed-up of the FA-LCP algorithm relative to Lemke's algorithm would grow in absolute terms when compared to the two-dimensional case. In general, we expect a three-dimensional problem to be bigger in terms of both global number of nodes n and local contact problems m. The overall scaling behaviour of the FA-LCP algorithm is dominated by the dense linear solve, scaling as $\mathcal{O}(m^3)$ as m grows larger. The (average-case) scaling behaviour of Lemke's algorithm is (notoriously) difficult to analyse, but it is known to have an exponential worst-case (Murty, 1980). Probabilistic arguments for LCPs with particular structure (random and sign invariant matrix $\boldsymbol{W}$) give $\mathcal{O}(m^2)$ pivots per step (Todd, 1986), and the pivoting operation scales with $\mathcal{O}(m^2)$, giving an overall scaling of $\mathcal{O}(m^4)$. However, our matrix $\boldsymbol{W}$ would not fulfil the random and sign-invariance properties, so this argument can only be taken to be indicative of the possible average-case scaling behaviour in a mechanical system. Taken at face value, this suggests a straightforward superiority of FA-LCP over Lemke in three dimensions, especially when considering that m is fixed for Lemke, but is expected to decrease with each iteration for FA-LCP. However, complicating this naive analysis is that three-dimensional geometries present many more opportunities for the heuristic that underlies FA-LCP to fail. Less favourable geometries where the correction of the displacement causes a different contact condition to trigger (as might easily happen in highly non-convex "jagged" geometries), elements being involved in multiple highly-coupled contact problems or strongly constrained local geometries causing updated displacements to remain in active contact are all much easier to achieve in three dimensions than two. As such, the size of the LCP solved at each iteration may not decrease as quickly in three dimensions as in two, limiting the relative numerical efficiency gain of FA-LCP over Lemke. It is also possible that in these more complicated geometries, the underlying heuristic results in a greater error than Lemke, due to incorrect discarding of contact pairs when constructing the reduced LCP, oscillation between multiple contact conditions or an insufficient number of iterations to solve the larger problem to a given tolerance.

Staying within two dimensional analysis, we may also note that the Coulomb friction model can be written in LCP form, following the classic approach of Stewart and Trinkle (1996), allowing a possible extension to the more realistic case of frictional contact. Cohesive zone models for fracture propagation (possibly inclusive of friction) can also naturally be implemented in this framework (Monerie and Acary, 2001; Collins-Craft et al., 2021, 2022; Collins-Craft and Acary, 2025). It is only in the case of friction (or cohesion) in three dimensions, where the problem cannot be written in LCP form, but instead as a second-order cone complementarity problem (Acary et al., 2024; Acary and Collins-Craft, 2025), where the FA-LCP method as presented in this paper to approximate the solution of the contact problem will not work, and further effort is required to develop a similar fast approximation method. We note that the numerical homogenisation by perturbation method remains robust in all of these cases, with the small caveat that formally as dissipative behaviours frictional sliding and crack growth should not be homogenised into elastic constants, but instead should appear as macro-scale plasticity.

6. Conclusion

In this study, a comprehensive FEM-based numerical framework is developed to analyse the behaviour of porous solids with frictionless solid contact in two dimensions. The framework incorporates a perturbation-based piecewise stiffness matrix updating scheme, enabling on-the-fly tracking of evolving incremental (tangent) effective anisotropic mechanical properties and poroelastic coefficients under multidirectional loading. The methodology is applied to both single-pore and multi-pore configurations to investigate the interplay between pore geometry, contact evolution, and macroscopic mechanical response. The main findings are summarised as follows:

1. The primary methodological contribution is FA-LCP, a fast approximation method for repeatedly solving the LCP arising from frictionless pore-wall contact. In the benchmark cases considered, FA-LCP reduced the contact-solution time by one to two orders of magnitude relative to the Lemke and projected Gauss–Seidel algorithms, while reproducing their global contact forces and homogenised stiffnesses within the reported numerical tolerances.
2. FA-LCP is embedded in a homogenisation framework which allows automated updates of stiffness parameters for evolving pore geometry, accurately capturing complex contact interactions and predicting anisotropic incremental tangent Young's modulus, shear modulus, Poisson's ratio, and inferred Biot coefficients under multidirectional loading. This method enables homogenisation of geometries that lack analytical solutions due to the strong interactions between the pores.
3. In both single- and multi-pore systems, progressive pore closure dominates the evolution of macroscopic mechanical properties rather than global porosity change. Sequential contact induces a transition from a skeleton-controlled deformation regime to a contact-network-dominated behaviour, highlighting that initial porosity alone cannot fully describe the material state.
4. Before solid contact, Young's modulus along the loading direction decreases with displacement, while the orthogonal modulus generally increases due to pore flattening. Shear loading induces asymmetric deformation and reduces Young's modulus

in all directions. After solid contact, the incremental tangent Young's moduli in different directions increase markedly, particularly under horizontal and vertical compression, where they progressively approach the Young's modulus of the intact solid.
5. Incremental tangent shear modulus initially increases during pore flattening due to enhanced oblique load transfer, and approaches to solid shear modulus after contact occurs. The incremental tangent Poisson's ratio exhibits decreases with displacement under compression, but can increase post-contact, especially under shear loading, reflecting inclined contact surfaces facilitating stress transfer and anisotropic coupling effects.
6. Inferred Biot coefficients exhibit strong directional dependence. They increase along the loading axis under uniaxial compression and rise in multiple directions under shear loading. Following solid contact, the Biot coefficients decrease greatly, particularly under compressive loading where they approach zero. This behaviour underscores the critical role of pore geometry, contact sequence, and emerging contact networks in governing poroelastic behaviour.

The framework presented in this article provides a robust and efficient tool for resolving complex contact interactions, capturing nonlinear, anisotropic, and path-dependent poromechanical responses that conventional FEM or continuum models cannot easily predict. By linking pore-scale mechanisms to macroscopic behaviour, it offers insights into stress redistribution, piecewise stiffness evolution, and poroelastic coupling, with direct relevance to both engineered porous materials and natural geological formations under multidirectional stress, laying the foundation for future studies on the design, optimisation, and mechanical stability assessment of porous systems.

CRediT authorship contribution statement

L. Zhang: Writing – original draft, Visualization, Software, Methodology, Investigation, Conceptualization. **N.A. Collins-Craft:** Writing – review & editing, Visualization, Methodology, Formal analysis. **P. Braun:** Writing – review & editing, Supervision, Resources, Project administration, Methodology, Funding acquisition, Conceptualization.

Declaration of competing interest

The authors declare that they have no known competing financial interests or personal relationships that could have appeared to influence the work reported in this paper.

Acknowledgements

This research is supported by French National Research Agency (Grant ANR-22-CPJ1-0027-01 Geosolutions to meet the climate change). L.Z. acknowledges the Alexander von Humboldt Foundation for financial support through the Humboldt Research Fellowship.

Appendix A. Derivations

A.1. State variables and powers

We consider a body $\Omega \in \mathbb{R}^3$ with boundaries denoted by Γ, where the initial position is defined by $\boldsymbol{X}$ and the current position $\boldsymbol{x}$. We consider that the geometry and properties of the system are invariant with respect to the x_2 variable (that is to say that we treat two-dimension problems with plane strain) and so the dimensionality of the system can be reduced with $\boldsymbol{x} = (x_1, x_3)$ (and similarly for $\boldsymbol{X}$). The displacement is then given by $\boldsymbol{u}(\boldsymbol{x}) = \boldsymbol{x} - \boldsymbol{X}$ and the velocity by $\boldsymbol{v} = \dot{\boldsymbol{u}}$, where the overdot indicates the derivative with respect to time. On the boundaries of the system, we may define a local orthonormal reference frame denoted $(\boldsymbol{x}, \boldsymbol{n}, \boldsymbol{t})$ where $\boldsymbol{n} \in \mathbb{R}^2$ is the normal unit vector pointing outwards from the surface, and the vector $\boldsymbol{t} \in \mathbb{R}^2$ is the tangent direction along the surface, positive in the direction that locally respects the right-hand rule. We may consider the relative normal displacement between two different points, both lying on a surface by $u_{\mathrm{N}}(\boldsymbol{x}^1, \boldsymbol{x}^2) = (\boldsymbol{u}(\boldsymbol{x}^1) - \boldsymbol{u}(\boldsymbol{x}^2)) \cdot \boldsymbol{n} \in \mathbb{R}$ where $\boldsymbol{n}$ is taken at $\boldsymbol{x}^1$. The relative normal velocity is then given by $v_{\mathrm{N}} = \dot{u}_{\mathrm{N}}$.

For a point lying on the surface of the body, the power of contact is given by

$$\mathcal{P}_{\mathrm{con}} = \int_{\Gamma} v_n r_{\mathrm{N}} \mathrm{d}x, \tag{52}$$

where r_{N} (≥ 0) is the contact pressure at the surface of the body by $r_{\mathrm{N}} = -(\boldsymbol{\sigma} \cdot \boldsymbol{n}) \cdot \boldsymbol{n}$, where $\boldsymbol{\sigma}$ is the (tension-positive) Cauchy stress. Then, we have the classical powers of the external, internal and inertial forces given by

$$\mathcal{P}_{\mathrm{ext}} = \int_{\Omega} \boldsymbol{v} \cdot \boldsymbol{f} \mathrm{d}x + \int_{\Gamma_{\mathcal{N}}} \boldsymbol{v} \cdot \boldsymbol{\tau} \mathrm{d}x, \tag{53}$$

$$\mathcal{P}_{\mathrm{int}} = -\int_{\Omega} \boldsymbol{\sigma} : \dot{\boldsymbol{\varepsilon}} \mathrm{d}x + \int_{\Gamma} v_n r_{\mathrm{N}} \mathrm{d}x, \tag{54}$$

$$\mathcal{P}_{\mathrm{acc}} = \int_{\Omega} \rho \boldsymbol{v} \cdot \dot{\boldsymbol{v}} \mathrm{d}x, \tag{55}$$

where $\boldsymbol{f}$ is the body force in Ω, $\boldsymbol{\tau}$ is the imposed surface traction on $\Gamma_{\mathcal{N}}$ (the region of the boundary that has the Neumann boundary condition applied), $\boldsymbol{\varepsilon} = \frac{1}{2}(\nabla \boldsymbol{u} + (\nabla \boldsymbol{u})^{\top})$ is the Cauchy strain, ρ is the mass density and $\dot{\boldsymbol{v}}$ is the acceleration. The principle of virtual power ensures that for any virtual velocities $\bar{\boldsymbol{v}}$, $\dot{\bar{\boldsymbol{\varepsilon}}}$ and $\bar{v}_{\mathrm{N}}$ the following holds:

$$\begin{aligned} \bar{\mathcal{P}}_{\mathrm{acc}} &= \bar{\mathcal{P}}_{\mathrm{ext}} + \bar{\mathcal{P}}_{\mathrm{int}}, \\ \int_{\Omega} \rho \bar{\boldsymbol{v}} \cdot \dot{\boldsymbol{v}} \mathrm{d}x &= \int_{\Omega} \bar{\boldsymbol{v}} \cdot \boldsymbol{f} \mathrm{d}x + \int_{\Gamma_{\mathcal{N}}} \bar{\boldsymbol{v}} \cdot \boldsymbol{\tau} \mathrm{d}x \\ &\quad - \int_{\Omega} \boldsymbol{\sigma} : \dot{\bar{\boldsymbol{\varepsilon}}} \mathrm{d}x + \int_{\Gamma} \bar{v}_n r_{\mathrm{N}} \mathrm{d}x. \end{aligned} \tag{56}$$

From here on we assume both that the system may be treated quasi-statically (that is, it evolves in time, but sufficiently slowly that the power of the inertial forces is zero), and that the relevant fields are sufficiently smooth away from contact boundaries. Localisation gives the equilibrium and boundary conditions of the system as

$$\begin{cases} \nabla \cdot \boldsymbol{\sigma} + \boldsymbol{f} = 0 & \text{in } \Omega, \\ \boldsymbol{\tau} = \boldsymbol{\sigma} \cdot \boldsymbol{n} & \text{on } \Gamma_{\mathcal{N}}, \\ \boldsymbol{u} = \boldsymbol{u}_D & \text{on } \Gamma_D, \\ r_{\mathrm{N}} = -(\boldsymbol{\sigma} \cdot \boldsymbol{n}) \cdot \boldsymbol{n} & \text{on } \Gamma \backslash \left(\Gamma_{\mathcal{N}} \cup \Gamma_D\right), \\ \Gamma_{\mathcal{N}} \cap \Gamma_D = \emptyset, \end{cases} \tag{57}$$

where Γ_D is the region of the boundary that has the Dirichlet boundary condition applied and u_D is the prescribed displacement.

A.2. Voigt notation

For convenience, we may transform the elastic stiffness tensor for full 3D isotropic elasticity, using Voigt notation, into a two-dimensional matrix given by

$$\boldsymbol{D}_s = \frac{E_s}{(1+\nu_s)(1-2\nu_s)} \begin{bmatrix} 1-\nu_s & \nu_s & \nu_s & 0 & 0 & 0 \\ \nu_s & 1-\nu_s & \nu_s & 0 & 0 & 0 \\ \nu_s & \nu_s & 1-\nu_s & 0 & 0 & 0 \\ 0 & 0 & 0 & \frac{1-2\nu_s}{2} & 0 & 0 \\ 0 & 0 & 0 & 0 & \frac{1-2\nu_s}{2} & 0 \\ 0 & 0 & 0 & 0 & 0 & \frac{1-2\nu_s}{2} \end{bmatrix}. \tag{58}$$

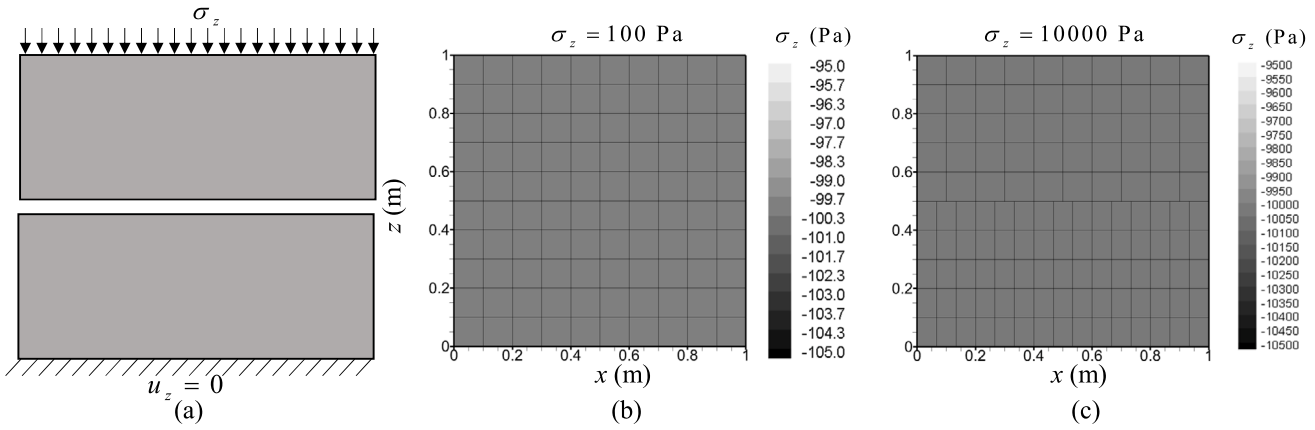


Fig. B.17. (a) Solid contact verification model with comparative analysis of (b) vertical stress distribution using matching elements across different solid parts and (c) vertical stress distribution using mismatching elements for different solid parts.

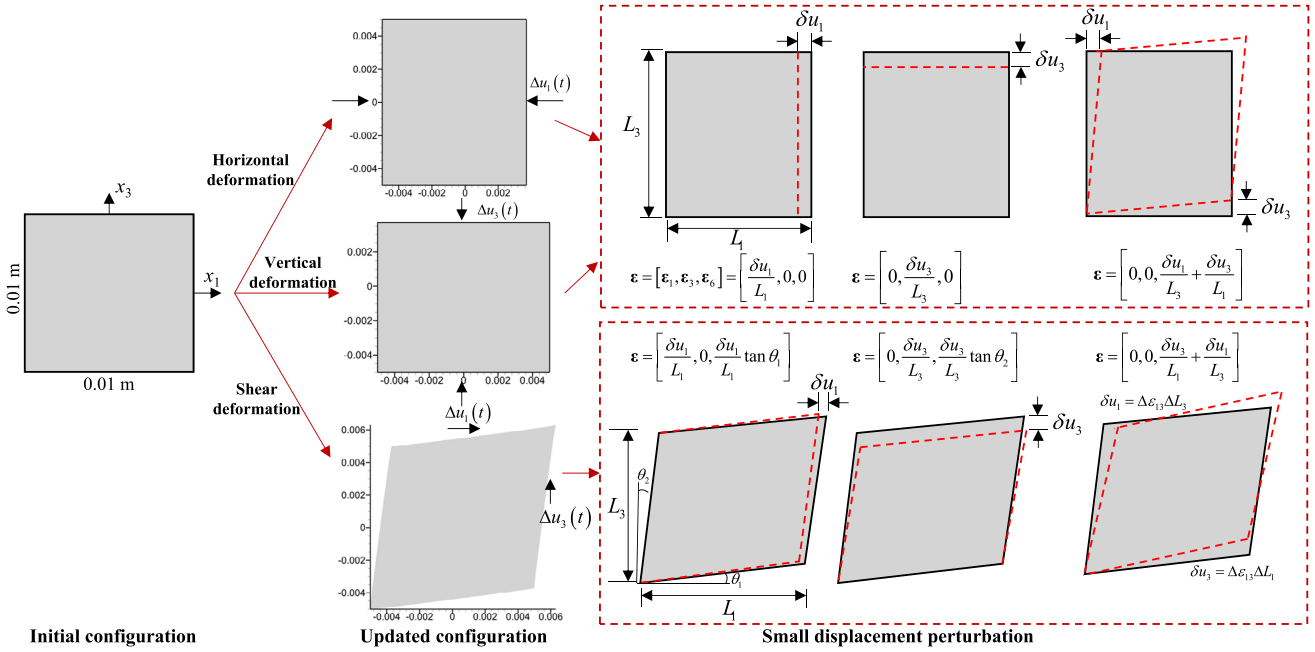


Fig. B.18. Square solid model ($L = 0.01$ m, $E_s = 54.2$ GPa and $\nu_s = 0.163$) undergoing continuous deformations with displacement perturbation methodology for updated stiffness matrix calculation.

Using the engineering Voigt notation, the strain and stress vectors are defined as

$$\boldsymbol{\varepsilon} = \begin{bmatrix}\varepsilon_1 & \varepsilon_2 & \varepsilon_3 & 2\varepsilon_4 & 2\varepsilon_5 & 2\varepsilon_6\end{bmatrix}^{\mathrm{T}},$$
$$\boldsymbol{\sigma} = \begin{bmatrix}\sigma_1 & \sigma_2 & \sigma_3 & \sigma_4 & \sigma_5 & \sigma_6\end{bmatrix}^{\mathrm{T}}. \tag{59}$$

A.3. Elasticity transformations

In order to transform between the elastic properties of the solid specified in (12) and the elastic properties of the overall RVE accounting for porosity, we exploit the formulas given in Charpin and Ehrlacher (2014):

$$E_1 = \frac{\left(\frac{D_{11}}{D_{31}}\right)^2 - \left(\frac{D_{13}}{D_{33}}\right)^2}{\frac{1}{D_{31}}\left(\frac{D_{11}}{D_{31}} + \frac{\nu_s^2}{E_2}\left[\left(\frac{D_{11}}{D_{31}}\right)^2 - 1\right]\right) + \frac{1}{D_{33}}\left(1 + \frac{\nu_s^2}{E_2}\left[1 - \left(\frac{D_{13}}{D_{33}}\right)^2\right]\right)}, \tag{60}$$

$$E_3 = \frac{\left(\frac{D_{33}}{D_{13}}\right)^2 - \left(\frac{D_{31}}{D_{11}}\right)^2}{\frac{1}{D_{11}}\left(1 + \frac{\nu_s^2}{E_2}\left[1 - \left(\frac{D_{31}}{D_{11}}\right)^2\right]\right) + \frac{1}{D_{31}}\left(\frac{D_{33}}{D_{13}} + \frac{\nu_s^2}{E_2}\left[\left(\frac{D_{33}}{D_{13}}\right)^2 - 1\right]\right)}, \tag{61}$$

and

$$\nu_{13} = \frac{D_{13}}{D_{33}} - \frac{E_1 \nu_s^2}{E_2}\left(\frac{D_{13}}{D_{33}} + 1\right), \tag{62}$$

$$G_{13} = D_{66}. \tag{63}$$

By incorporating these into the stiffness matrix formulation, we obtain

$$D_{13} = D_{31}, \tag{64}$$
$$D_{23} = D_{32}, \tag{65}$$
$$\frac{\nu_{13}}{E_1} = \frac{\nu_{31}}{E_3}, \tag{66}$$
$$\frac{\nu_{23}}{E_2} = \frac{\nu_{32}}{E_3}. \tag{67}$$

We can thus also determine D_{22}:

$$D_{22} = \frac{{E_2}^2 E_3 (E_1 - {\nu_{13}}^2 E_3)}{E_1 E_2 E_3 - {E_1}^2 E_2 {\nu_s}^2 - {\nu_{13}}^2 E_2 {E_3}^2 - E_1 {E_3}^2 {\nu_s}^2 - 2 E_1 {E_3}^2 \nu_{13} {\nu_s}^2}. \tag{68}$$

Appendix B. Validation

B.1. Simple face-to-face contact validation

To validate the accuracy of the contact detection, classification, and contact model, a face-to-face contact test is simulated, as shown in Fig. B.17(a). Two separate solids subjected to vertical normal stress σ_3 are analysed, to simulate contact-induced internal vertical stress distributions. The test is conducted using matching elements (with aligned nodes across the contact surface) in Fig. B.17(b) and mismatching elements (where nodes do not in general align across the contact surface) in Fig. B.17(c) while applying different vertical stress boundary conditions. The results demonstrate that the internal vertical stress computed by the simulator in Fig. 2 aligns with the applied stress boundary conditions across the different models.

B.2. Validation of numerical homogenisation

To verify the updated stiffness matrix obtained via the perturbation method, a simple square solid model with side length of 10 mm is simulated. The verification procedure consists of two steps, as shown in Fig. B.18. First, prescribed displacements are applied to the model, leading to a modified configuration. Then, based on the updated configuration, small displacement perturbations are introduced to generate small additional strains and compute the updated stiffness matrix. It should be noted that a single displacement perturbation does not necessarily correspond to a single strain component, since shear displacements may induce asymmetry in the model. However, the numerical results show that the stiffness matrix remains symmetric under displacements in different directions. The computed stiffness components are $D_{11} = D_{33} = 57.9$ GPa, $D_{21} = D_{31} = D_{13} = D_{23} = 11.3$ GPa, $D_{66} = 23.3$ GPa and the other components are 0. The calculated stiffness matrix is consistent with the isotropic elastic stiffness matrix derived directly from E_s and ν_s, validating the effectiveness of the perturbation method in updating mechanical properties.

Appendix C. Supplementary data

Supplementary material related to this article can be found online at https://doi.org/10.1016/j.compgeo.2026.108762.

Data availability

Data will be made available on request.

References

Acary, V., Armand, P., Nguyen, H., Shpakovych, M., 2024. Second-order cone programming for frictional contact mechanics using interior point algorithm. Optim. Methods Softw. 1–30. http://dx.doi.org/10.1080/10556788.2023.2296438, URL: https://www.tandfonline.com/doi/full/10.1080/10556788.2023.2296438.

Acary, V., Bonnefon, O., Brémond, M., Huber, O., Sinclair, S., 2019. An Introduction to Siconos. Technical Report, INRIA, URL: https://inria.hal.science/inria-00162911v3.

Acary, V., Bourrier, F., Viano, B., 2023. Variational approach for nonsmooth elastoplastic dynamics with contact and impacts. Comput. Methods Appl. Mech. Engrg. 414, 116156. http://dx.doi.org/10.1016/j.cma.2023.116156, URL: https://www.sciencedirect.com/science/article/pii/S0045782523002803.

Acary, V., Collins-Craft, N., 2025. On the Moreau–Jean scheme with the Frémond impact law: Energy conservation and dissipation properties for elastodynamics with contact, impact and friction. J. Theor. Comput. Appl. Mech. 1–29. http://dx.doi.org/10.46298/jtcam.13480, URL: https://hal.science/hal-04230941.

Ahmed, S., Müller, T., Madadi, M., Calo, V., 2019. Drained pore modulus and Biot coefficient from pore-scale digital rock simulations. Int. J. Rock Mech. Min. Sci. 114, 62–70. http://dx.doi.org/10.1016/j.ijrmms.2018.12.019, URL: https://linkinghub.elsevier.com/retrieve/pii/S1365160918300959.

Batistić, I., Cardiff, P., Tuković, v.Z., 2022. A finite volume penalty based segment-to-segment method for frictional contact problems. Appl. Math. Model. 101, 673–693. http://dx.doi.org/10.1016/j.apm.2021.09.009, URL: https://linkinghub.elsevier.com/retrieve/pii/S0307904X21004248.

Batzle, M., Simmons, G., Siegfried, R., 1980. Microcrack closure in rocks under stress: Direct observation. J. Geophys. Res.: Solid Earth 85, 7072–7090. http://dx.doi.org/10.1029/JB085iB12p07072, URL: https://onlinelibrary.wiley.com/doi/abs/10.1029/JB085iB12p07072.

Biot, M., 1941. General theory of three-dimensional consolidation. J. Appl. Phys. 12, 155–164. http://dx.doi.org/10.1063/1.1712886, URL: https://pubs.aip.org/jap/article/12/2/155/141365/General-Theory-of-Three-Dimensional-Consolidation.

Biot, M., 1973. Nonlinear and semilinear rheology of porous solids. J. Geophys. Res. (1896-1977) 78, 4924–4937. http://dx.doi.org/10.1029/JB078i023p04924, URL: https://onlinelibrary.wiley.com/doi/abs/10.1029/JB078i023p04924.

Brogliato, B., 2016. Nonsmooth Mechanics: Models, Dynamics and Control. Communications and Control Engineering. Springer International Publishing, Cham, http://dx.doi.org/10.1007/978-3-319-28664-8, URL: http://link.springer.com/10.1007/978-3-319-28664-8.

Capobianco, G., Eugster, S., 2016. A Moreau-type variational integrator. PAMM 16, 941–944. http://dx.doi.org/10.1002/pamm.201610453, URL: https://onlinelibrary.wiley.com/doi/abs/10.1002/pamm.201610453.

Capobianco, G., Eugster, S., 2018. Time finite element based Moreau-type integrators. Internat. J. Numer. Methods Engrg. 114, 215–231. http://dx.doi.org/10.1002/nme.5741, URL: https://onlinelibrary.wiley.com/doi/abs/10.1002/nme.5741.

Capobianco, G., Eugster, S., Leine, R., 2017. Moreau-type integrators based on the time finite element discretization of the virtual action. PAMM 17, 143–144. http://dx.doi.org/10.1002/pamm.201710041, URL: https://onlinelibrary.wiley.com/doi/abs/10.1002/pamm.201710041.

Charpin, L., Ehrlacher, A., 2014. Estimating the poroelastic properties of cracked materials. Acta Mech. 225, 2501–2519. http://dx.doi.org/10.1007/s00707-013-1082-0.

Collins-Craft, N., Acary, V., 2025. On the formulation and implementation of mixed mode I and mode II extrinsic cohesive zone models with contact and friction. URL: https://inria.hal.science/hal-04447397.

Collins-Craft, N., Bourrier, F., Acary, V., 2021. An extrinsic cohesive zone model with contact developed in the non-smooth mechanics framework. In: 33rd Nordic Seminar on Computational Mechanics. Jönköping, p. 1, URL: https://congress.cimne.com/NSCM-33/Admin/Files/FileAbstract/a17.pdf.

Collins-Craft, N., Bourrier, F., Acary, V., 2022. On the formulation and implementation of extrinsic cohesive zone models with contact. Comput. Methods Appl. Mech. Engrg. 400, 115545. http://dx.doi.org/10.1016/j.cma.2022.115545, URL: https://www.sciencedirect.com/science/article/pii/S0045782522005369.

Cottle, R., Pang, J.S., Stone, R., 2009. The Linear Complementarity Problem. Classics in Applied Mathematics. Society for Industrial and Applied Mathematics, Philadelphia, http://dx.doi.org/10.1137/1.9780898719000, URL: http://epubs.siam.org/doi/book/10.1137/1.9780898719000.

Coussy, O., 2004. Poromechanics, second ed. Wiley, Chichester, England ; Hoboken, NJ, http://dx.doi.org/10.1002/0470092718, URL: https://onlinelibrary.wiley.com/doi/book/10.1002/0470092718.

Dehghani, H., Zilian, A., 2020. Poroelastic model parameter identification using artificial neural networks: On the effects of heterogeneous porosity and solid matrix Poisson ratio. Comput. Mech. 66, 625–649. http://dx.doi.org/10.1007/s00466-020-01868-4, URL: https://doi.org/10.1007/s00466-020-01868-4.

Dubois, F., Acary, V., Jean, M., 2018. The contact dynamics method: A nonsmooth story. C. R. Méc. 346, 247–262. http://dx.doi.org/10.1016/j.crme.2017.12.009, URL: https://linkinghub.elsevier.com/retrieve/pii/S163107211730236X.

Elishakoff, I., Ren, Y., Shinozuka, M., 1997. New formulation of FEM for deterministic and stochastic beams through generalization of Fuchs' approach. Comput. Methods Appl. Mech. Engrg. 144, 235–243. http://dx.doi.org/10.1016/S0045-7825(96)01173-5, URL: https://linkinghub.elsevier.com/retrieve/pii/S0045782596011735.

Eshelby, J., 1957. The determination of the elastic field of an ellipsoidal inclusion, and related problems. Proc. R. Soc. Lond. Ser. A. Math. Phys. Sci. 241, 376–396. http://dx.doi.org/10.1098/rspa.1957.0133, URL: https://royalsocietypublishing.org/doi/abs/10.1098/rspa.1957.0133.

Fischer, A., 1992. A special Newton-type optimization method. Optimization 24, 269–284. http://dx.doi.org/10.1080/02331939208843795, URL: http://www.tandfonline.com/doi/abs/10.1080/02331939208843795.

Fischer, A., 1995. A Newton-type method for positive-semidefinite linear complementarity problems. J. Optim. Theory Appl. 86, 585–608. http://dx.doi.org/10.1007/BF02192160, URL: http://link.springer.com/10.1007/BF02192160.

Fischer, A., 1997. Solution of monotone complementarity problems with locally lipschitzian functions. Math. Program. 76, 513–532. http://dx.doi.org/10.1007/BF02614396.

Frémond, M., 2002. Non-Smooth Thermomechanics. Springer Berlin Heidelberg, http://dx.doi.org/10.1007/978-3-662-04800-9, URL: http://link.springer.com/10.1007/978-3-662-04800-9.

Geers, M., Kouznetsova, V., Brekelmans, W., 2010. Multi-scale computational homogenization: Trends and challenges. J. Comput. Appl. Math. 234, 2175–2182. http://dx.doi.org/10.1016/j.cam.2009.08.077, URL: https://linkinghub.elsevier.com/retrieve/pii/S0377042709005536.

Hashin, Z., 1985. Large isotropic elastic deformation of composites and porous media. Int. J. Solids Struct. 21, 711–720. http://dx.doi.org/10.1016/0020-7683(85)90074-5, URL: https://linkinghub.elsevier.com/retrieve/pii/0020768385900745.

Hill, R., 1963. Elastic properties of reinforced solids: Some theoretical principles. J. Mech. Phys. Solids 11, 357–372. http://dx.doi.org/10.1016/0022-5096(63)90036-X, URL: https://linkinghub.elsevier.com/retrieve/pii/002250966390036X.

Hill, R., 1965. A self-consistent mechanics of composite materials. J. Mech. Phys. Solids 13, 213–222. http://dx.doi.org/10.1016/0022-5096(65)90010-4, URL: https://linkinghub.elsevier.com/retrieve/pii/0022509665900104.

Jean, M., 1999. The non-smooth contact dynamics method. Comput. Methods Appl. Mech. Engrg. 177, 235–257. http://dx.doi.org/10.1016/S0045-7825(98)00383-1, URL: https://linkinghub.elsevier.com/retrieve/pii/S0045782598003831.

Jourdan, F., Alart, P., Jean, M., 1998. A Gauss-Seidel like algorithm to solve frictional contact problems. Comput. Methods Appl. Mech. Engrg. 155, 31–47. http://dx.doi.org/10.1016/S0045-7825(97)00137-0, URL: https://www.sciencedirect.com/science/article/pii/S0045782597001370.

Kachanov, M., Tsukrov, I., Shafiro, B., 1994. Effective moduli of solids with cavities of various shapes. Appl. Mech. Rev. 47, S151–S174. http://dx.doi.org/10.1115/1.3122810, URL: https://asmedigitalcollection.asme.org/appliedmechanicsreviews/article/47/1S/S151/401239/Effective-Moduli-of-Solids-With-Cavities-of.

Kanit, T., Forest, S., Galliet, I., Mounoury, V., Jeulin, D., 2003. Determination of the size of the representative volume element for random composites: Statistical and numerical approach. Int. J. Solids Struct. 40, 3647–3679. http://dx.doi.org/10.1016/S0020-7683(03)00143-4, URL: https://linkinghub.elsevier.com/retrieve/pii/S0020768303001434.

Kanouté, P., Boso, D., Chaboche, J., Schrefler, B., 2009. Multiscale methods for composites: A review. Arch. Comput. Methods Eng. 16, 31–75. http://dx.doi.org/10.1007/s11831-008-9028-8, URL: https://doi.org/10.1007/s11831-008-9028-8.

Kouznetsova, V., Brekelmans, W., Baaijens, F., 2001. An approach to micro-macro modeling of heterogeneous materials. Comput. Mech. 27, 37–48. http://dx.doi.org/10.1007/s004660000212.

Larsson, F., Runesson, K., Saroukhani, S., Vafadari, R., 2011. Computational homogenization based on a weak format of micro-periodicity for RVE-problems. Comput. Methods Appl. Mech. Engrg. 200, 11–26. http://dx.doi.org/10.1016/j.cma.2010.06.023, URL: https://linkinghub.elsevier.com/retrieve/pii/S0045782510001908.

Lee, E., Goh, T., Lee, J., Heo, J.Y., Kim, G.B., Lee, C.S., 2019. Experimental investigation of macroscopic material nonlinear behavior and microscopic void volume fraction change for porous materials under uniaxial compression. Compos. Part B: Eng. 163, 130–138. http://dx.doi.org/10.1016/j.compositesb.2018.11.019, URL: https://linkinghub.elsevier.com/retrieve/pii/S1359836818311922.

Lemke, C., 1965. Bimatrix equilibrium points and mathematical programming. Manag. Sci. 11, 681–689. http://dx.doi.org/10.1287/mnsc.11.7.681, URL: http://pubsonline.informs.org/doi/abs/10.1287/mnsc.11.7.681.

Lemke, C., Howson, Jr., J., 1964. Equilibrium points of bimatrix games. J. Soc. Ind. Appl. Math. 12, 413–423. http://dx.doi.org/10.1137/0112033, URL: http://epubs.siam.org/doi/10.1137/0112033.

Lydzba, D., Shao, J., 2000. Study of poroelasticity material coefficients as response of microstructure. Mech. Cohesive-Frictional Mater. 5, 149–171. http://dx.doi.org/10.1002/(SICI)1099-1484(200002)5:2<149::AID-CFM89>3.0.CO;2-F, URL: https://onlinelibrary.wiley.com/doi/abs/10.1002/%28SICI%291099-1484%28200002%295%3A2%3C149%3A%3AAID-CFM89%3E3.0.CO%3B2-F.

Mandel, J., 1971. Plasticite classique et viscoplasticite. In: CISM International Centre for Mechanical Sciences, vol. 565, Springer International Publishing, Cham.

Miehe, C., 2003. Computational micro-to-macro transitions for discretized microstructures of heterogeneous materials at finite strains based on the minimization of averaged incremental energy q. Comput. Methods Appl. Mech. Engrg. 192, 559–591. http://dx.doi.org/10.1016/S0045-7825(02)00564-9, URL: https://www.sciencedirect.com/science/article/pii/S0045782502005649.

Miehe, C., Koch, A., 2002. Computational micro-to-macro transitions of discretized microstructures undergoing small strains. Arch. Appl. Mech. 72, 300–317. http://dx.doi.org/10.1007/s00419-002-0212-2.

Monerie, Y., Acary, V., 2001. Formulation dynamique d'un modèle de zone cohésive tridimensionnel couplant endommagement et frottement. Rev. Eur. Élém. Finis 10, 489–503. http://dx.doi.org/10.1080/12506559.2001.11869264, URL: https://www.tandfonline.com/doi/full/10.1080/12506559.2001.11869264.

Mori, T., Tanaka, K., 1973. Average stress in matrix and average elastic energy of materials with misfitting inclusions. Acta Metall. 21, 571–574. http://dx.doi.org/10.1016/0001-6160(73)90064-3, URL: https://www.sciencedirect.com/science/article/pii/0001616073900643.

Murty, K., 1980. Computational complexity of parametric linear programming. Math. Program. 19, 213–219. http://dx.doi.org/10.1007/BF01581642, URL: http://link.springer.com/10.1007/BF01581642.

Nemat-Nasser, S., Hori, M., 1998. Micromechanics: Overall properties of heterogeneous materials, second ed. In: North-Holland Series in Applied Mathematics and Mechanics, vol. 37, North-Holland, Amsterdam.

Nguyen, V.D., Béchet, E., Geuzaine, C., Noels, L., 2012. Imposing periodic boundary condition on arbitrary meshes by polynomial interpolation. Comput. Mater. Sci. 55, 390–406. http://dx.doi.org/10.1016/j.commatsci.2011.10.017, URL: https://linkinghub.elsevier.com/retrieve/pii/S0927025611005866.

Papadopoulos, P., Solberg, J., 1998. A Lagrange multiplier method for the finite element solution of frictionless contact problems. Math. Comput. Modelling 28, 373–384. http://dx.doi.org/10.1016/s0895-7177(98)00128-9, URL: https://linkinghub.elsevier.com/retrieve/pii/S0895717798001289.

Perić, D., Owen, D., 1992. Computational model for 3-D contact problems with friction based on the penalty method. Internat. J. Numer. Methods Engrg. 35, 1289–1309. http://dx.doi.org/10.1002/nme.1620350609, URL: https://onlinelibrary.wiley.com/doi/abs/10.1002/nme.1620350609.

Ponte Castañeda, P., Zaidman, M., 1994. Constitutive models for porous materials with evolving microstructure. J. Mech. Phys. Solids 42, 1459–1497. http://dx.doi.org/10.1016/0022-5096(94)90005-1, URL: https://linkinghub.elsevier.com/retrieve/pii/0022509694900051.

Rohan, E., Heczko, J., 2020. Homogenization and numerical modelling of poroelastic materials with self-contact in the microstructure. Comput. Struct. 230, 106086. http://dx.doi.org/10.1016/j.compstruc.2019.06.003, URL: https://linkinghub.elsevier.com/retrieve/pii/S0045794919300264.

Rohan, E., Heczko, J., 2023. Homogenization and numerical algorithms for two-scale modeling of porous media with self-contact in micropores. J. Comput. Appl. Math. 432, 115276. http://dx.doi.org/10.1016/j.cam.2023.115276, URL: https://www.sciencedirect.com/science/article/pii/S0377042723002200.

Rohan, E., Heczko, J., 2026. Homogenization-based modelling of self-contact and fluid-structure interaction in the microstructure of poroelastic materials. Comput. Struct. 322, 108089. http://dx.doi.org/10.1016/j.compstruc.2025.108089, URL: https://www.sciencedirect.com/science/article/pii/S004579492500447X.

Sahimi, M., 1993. Flow phenomena in rocks: From continuum models to fractals, percolation, cellular automata, and simulated annealing. Rev. Modern Phys. 65, 1393–1534. http://dx.doi.org/10.1103/RevModPhys.65.1393, URL: https://link.aps.org/doi/10.1103/RevModPhys.65.1393.

Schenk, O., Gärtner, K., 2004. Solving unsymmetric sparse systems of linear equations with PARDISO. Future Gener. Comput. Syst. 20, 475–487. http://dx.doi.org/10.1016/j.future.2003.07.011, URL: https://linkinghub.elsevier.com/retrieve/pii/S0167739X03001882.

Smeets, S., Renaud, N., Van Willenswaard, L., 2022. Nanomesh: A Python workflow tool for generating meshesfrom image data. J. Open Source Softw. 7, 4654. http://dx.doi.org/10.21105/joss.04654, URL: https://joss.theoj.org/papers/10.21105/joss.04654.

Stewart, D., Trinkle, J., 1996. An implicit time-stepping scheme for rigid body dynamics with inelastic collisions and Coulomb Friction. Internat. J. Numer. Methods Engrg. 39, 2673–2691. http://dx.doi.org/10.1002/(SICI)1097-0207(19960815)39:15<2673::AID-NME972>3.0.CO;2-I, URL: https://onlinelibrary.wiley.com/doi/10.1002/(SICI)1097-0207(19960815)39:15%3C2673::AID-NME972%3E3.0.CO;2-I.

Tan, X., Konietzky, H., 2014. Numerical study of variation in Biot's coefficient with respect to microstructure of rocks. Tectonophysics 610, 159–171. http://dx.doi.org/10.1016/j.tecto.2013.11.014, URL: https://linkinghub.elsevier.com/retrieve/pii/S0040195113006616.

Tang, Y., Yao, X., Chen, Y., Zhou, Y., Zhu, D., Zhang, Y., Zhang, T., Peng, Y., 2020. Experiment research on physical clogging mechanism in the porous media and its impact on permeability. Granul. Matter 22, 37. http://dx.doi.org/10.1007/s10035-020-1001-8.

Temizer, I., Wriggers, P., 2008. On the computation of the macroscopic tangent for multiscale volumetric homogenization problems. Comput. Methods Appl. Mech. Engrg. 198, 495–510. http://dx.doi.org/10.1016/j.cma.2008.08.018, URL: https://linkinghub.elsevier.com/retrieve/pii/S0045782508003149.

Terada, K., Hori, M., Kyoya, T., Kikuchi, N., 2000. Simulation of the multi-scale convergence in computational homogenization approaches. Int. J. Solids Struct. 37, 2285–2311. http://dx.doi.org/10.1016/S0020-7683(98)00341-2, URL: https://linkinghub.elsevier.com/retrieve/pii/S0020768398003412.

Thorpe, M., Sen, P., 1985. Elastic moduli of two-dimensional composite continua with elliptical inclusions. J. Acoust. Soc. Am. 77, 1674–1680. http://dx.doi.org/10.1121/1.391966.

Todd, M., 1986. Polynomial expected behavior of a pivoting algorithm for linear complementarity and linear programming problems. Math. Program. 35, 173–192. http://dx.doi.org/10.1007/BF01580646.

Tsukrov, I., Kachanov, M., 2000. Effective moduli of an anisotropic material with elliptical holes of arbitrary orientational distribution. Int. J. Solids Struct. 37, 5919–5941. http://dx.doi.org/10.1016/S0020-7683(99)00244-9, URL: https://www.sciencedirect.com/science/article/pii/S0020768399002449.

Wriggers, P., 1995. Finite element algorithms for contact problems. Arch. Comput. Methods Eng. 2, 1–49. http://dx.doi.org/10.1007/BF02736195, URL: https://link.springer.com/article/10.1007/BF02736195.

Yastrebov, V.A., 2013. Numerical Methods in Contact Mechanics. Numerical Methods in Engineering Series. Hoboken, NJ, ISTE ; Wiley, London, http://dx.doi.org/10.1002/9781118647974, URL: https://onlinelibrary.wiley.com/doi/book/10.1002/9781118647974.